Author(s): ALICE Collaboration

Title: Measurement of transverse energy at midrapidity in Pb-Pb collisions at √sNN = 2.76 TeV

Year: 2016

Version:

Measurement of transverse energy at midrapidity in Pb-Pb collisions at $\sqrt{s_{NN}} = 2.76$ TeV

J. Adam *et al.**

(ALICE Collaboration)

We report the transverse energy (E_T) measured with ALICE at midrapidity in Pb-Pb collisions at $\sqrt{s_{NN}} =$ 2.76 TeV as a function of centrality. The transverse energy was measured using identified single-particle tracks. The measurement was cross checked using the electromagnetic calorimeters and the transverse momentum distributions of identified particles previously reported by ALICE. The results are compared to theoretical models as well as to results from other experiments. The mean E_T per unit pseudorapidity (η), $\langle dE_T/d\eta \rangle$, in 0%–5% central collisions is $1737 \pm 6(\text{stat.}) \pm 97(\text{sys.})$ GeV. We find a similar centrality dependence of the shape of $\langle dE_T/d\eta \rangle$ as a function of the number of participating nucleons to that seen at lower energies. The growth in $\langle dE_T/d\eta \rangle$ at the LHC energies exceeds extrapolations of low-energy data. We observe a nearly linear scaling of $\langle dE_T/d\eta \rangle$ with the number of quark participants. With the canonical assumption of a 1 fm/c formation time, we estimate that the energy density in 0%–5% central Pb-Pb collisions at $\sqrt{s_{NN}} = 2.76$ TeV is 12.3 ± 1.0 GeV/fm^3 and that the energy density at the most central 80 fm^2 of the collision is at least 21.5 ± 1.7 GeV/fm^3. This is roughly 2.3 times that observed in 0%–5% central Au-Au collisions at $\sqrt{s_{NN}} = 200$ GeV.

I. INTRODUCTION

Quantum chromodynamics (QCD) predicts a phase transition of nuclear matter to a plasma of quarks and gluons at energy densities above about 0.2–1 GeV/fm^3 [1,2]. This matter, called quark-gluon plasma (QGP), is produced in high-energy nuclear collisions [3–17] and its properties are being investigated at the Super Proton Synchrotron (SPS), the Relativistic Heavy Ion Collider (RHIC), and the Large Hadron Collider (LHC). The highest energy densities are achieved at the LHC in Pb-Pb collisions.

The mean transverse energy per unit pseudorapidity $\langle dE_T/d\eta \rangle$ conveys information about how much of the initial longitudinal energy carried by the incoming nuclei is converted into energy carried by the particles produced transverse to the beam axis. The transverse energy at midrapidity is therefore a measure of the stopping power of nuclear matter. By using simple geometric considerations [18] $\langle dE_T/d\eta \rangle$ can provide information on the energy densities attained. Studies of the centrality and $\sqrt{s_{NN}}$ dependence of $\langle dE_T/d\eta \rangle$ therefore provide insight into the conditions prior to thermal and chemical equilibrium.

The $\langle dE_T/d\eta \rangle$ has been measured at the BNL Alternating Gradient Synchrotron by E802 [19] and E814/E877 [20]; at the SPS by NA34 [21], NA35 [22], NA49 [23], and WA80/93/98 [24,25]; at RHIC by PHENIX [26–28] and STAR [29]; and at the LHC by CMS [30], covering nearly three orders of magnitude of $\sqrt{s_{NN}}$. The centrality dependence has also been studied extensively with $\langle dE_T/d\eta \rangle$ at midrapidity scaling nearly linearly with the collision volume, or equivalently, the number of participating nucleons at lower energies [24,31,32]. Further studies of heavy-ion collisions revealed deviations from this simple participant scaling law [25]. The causes of this deviation from linearity are still actively discussed and might be related to effects from minijets [33,34] or constituent quark scaling [28,35].

The ALICE detector [36] has precision tracking detectors and electromagnetic calorimeters, enabling several different methods for measuring E_T. In this paper we discuss measurements of $\langle dE_T/d\eta \rangle$ in Pb-Pb collisions at $\sqrt{s_{NN}} = 2.76$ TeV using the tracking detectors alone and using the combined information from the tracking detectors and the electromagnetic calorimeters. In addition we compare to calculations of $\langle dE_T/d\eta \rangle$ from the measured identified particle transverse momentum distributions. Measurements from the tracking detectors alone provide the highest precision. We compare our results to theoretical calculations and measurements at lower energies.

II. EXPERIMENT

A comprehensive description of the ALICE detector can be found in Ref. [36]. This analysis uses the V0, zero-degree calorimeters (ZDCs), the inner tracking system (ITS), the time projection chamber (TPC), the electromagnetic calorimeter (EMCal), and the photon spectrometer (PHOS), all of which are located inside a 0.5-T solenoidal magnetic field. The V0 detector [37] consists of two scintillator hodoscopes covering the pseudorapidity ranges $-3.7 < \eta < -1.7$ and $2.8 < \eta < 5.1$. The ZDCs each consist of a neutron calorimeter between the beam pipes downstream of the dipole magnet and a proton calorimeter external to the outgoing beam pipe.

The TPC [38], the main tracking detector at midrapidity, is a cylindrical drift detector filled with a Ne-CO$_2$ gas mixture. The active volume is nearly 90 m^3 and has inner and outer radii of 0.848 and 2.466 m, respectively. It provides particle

---

identification via the measurement of the specific ionization energy loss (dE/dx) with a resolution of 5.2% and 6.5% in peripheral and central collisions, respectively.

The ITS [36] consists of the silicon pixel detector with layers at radii of 3.9 and 7.6 cm, the silicon drift detector with layers at radii of 15.0 and 23.9 cm, and the silicon strip detector with layers at radii of 38.0 and 43.0 cm. The TPC and ITS are aligned to within a few hundred μm using cosmic ray and *pp* collision data [39].

The EMCal [40,41] is a lead/scintillator sampling calorimeter covering $|\eta| < 0.7$ in pseudorapidity and $100°$ in azimuth in 2011. The EMCal consists of 11 520 towers, each with transverse size 6×6 cm, or approximately twice the effective Molière radius. The relative energy resolution is $\sqrt{0.11^2/E + 0.017^2}$, where the energy E is measured in GeV [40]. Clusters are formed by combining signals from adjacent towers. Each cluster is required to have only one local energy maximum. Noise is suppressed by requiring a minimum tower energy of 0.05 GeV. For this analysis we use clusters within $|\eta| < 0.6$. The PHOS [42] is a lead tungstate calorimeter covering $|\eta| < 0.12$ in pseudorapidity and $60°$ in azimuth. The PHOS consists of three modules of 64×56 towers each, with each tower having a transverse size of 2.2×2.2 cm, comparable to the Molière radius. The relative energy resolution is $\sqrt{0.013^2/E^2 + 0.036^2/E + 0.01^2}$, where the energy E is measured in GeV [43].

The minimum-bias trigger for Pb-Pb collisions in 2010 was defined by a combination of hits in the V0 detector and the two innermost (pixel) layers of the ITS [8]. In 2011 the minimum-bias trigger signals in both neutron ZDCs were also required [44]. The collision centrality is determined by comparing the multiplicity measured in the V0 detector to Glauber model simulations of the multiplicity [8,37]. These calculations are also used to determine the number of participating nucleons, $\langle N_{\mathrm{part}} \rangle$. We restrict our analysis to the 0%–80% most central collisions. For these centralities corrections owing to electromagnetic interactions and trigger inefficiencies are negligible. We use data from approximately 70 000 0%–80% central events taken in 2011 for the tracking detector and EMCal measurements and data from approximately 600 000 0%–80% central events taken in 2010 for the PHOS measurement. We focus on a small event sample where the detector performance was uniform to simplify efficiency corrections because the measurement is dominated by systematic uncertainties.

Tracks are reconstructed using both the TPC and the ITS. Tracks are selected by requiring that they cross at least 70 rows and requiring a χ^2 per space point <4. Tracks are restricted to $|\eta| < 0.6$. Each track is required to have at least one hit in one of the two innermost ITS layers and a small distance of closest approach (DCA) to the primary vertex in the xy plane as a function of transverse momentum (p_{T}), defined by $\mathrm{DCA}_{xy} < (0.0182 + 0.035/p_{\mathrm{T}}^{1.01})$ cm, where p_{T} is in GeV/c. The distance of closest approach in the z direction is restricted to $\mathrm{DCA}_z < 2$ cm. This reduces the contribution from secondary particles from weak decays, which appear as a background. With these selection criteria tracks with transverse momenta $p_{\mathrm{T}} > 150$ MeV/c can be reconstructed.

The typical momentum resolution for low-momentum tracks, which dominate E_{T} measurements, is $\Delta p_{\mathrm{T}}/p_{\mathrm{T}} \approx 1\%$. The reconstruction efficiency varies with p_{T} and ranges from about 50% to 75% [44].

Particles are identified through their specific energy loss, dE/dx, in the TPC when possible. The dE/dx is calculated using a truncated-mean procedure and compared to the dE/dx expected for a given particle species using a Bethe-Bloch parametrization. The deviation from the expected dE/dx value is expressed in units of the energy-loss resolution σ [45]. Tracks are identified as arising from a kaon if they are within 3σ from the expected dE/dx for a kaon, more than 3σ from the expected dE/dx for a proton or a pion, and have $p_{\mathrm{T}} < 0.45$ GeV/c. Tracks are identified as arising from (anti)protons if they are within 3σ from the expected dE/dx for (anti)protons, more than 3σ from the expected dE/dx for kaons or pions, and have $p_{\mathrm{T}} < 0.9$ GeV/c. Tracks are identified as arising from an electron (positron) and therefore excluded from the measurement of $E_{\mathrm{T}}^{\pi,K,p}$ if they are within 2σ from the expected dE/dx for an electron (positron), more than 4σ from the expected dE/dx for a pion, and more than 3σ from the expected dE/dx for a proton or kaon. With this algorithm approximately 0.1% of tracks arise from electrons or positrons misidentified as arising from pions and fewer than 0.1% of tracks are misidentified as arising from kaons or protons. Any track not identified as a kaon or proton is assumed to arise from a pion and the measurement must be corrected for the error in this assumption.

The PHOS and EMCal are used to measure the electromagnetic energy component of the E_{T} and to demonstrate consistency between methods. Data from 2011 were used for the EMCal analysis owing to the larger EMCal acceptance in 2011. Data from one run in 2010 were used for the PHOS owing to better detector performance and understanding of the calibrations in that run period. The EMCal has a larger acceptance, but the PHOS has a better energy resolution. There is also a lower material budget in front of the PHOS than the EMCal. This provides an additional check on the accuracy of the measurement.

III. METHOD

Historically, most E_{T} measurements have been performed using calorimeters, and the commonly accepted operational definition of E_{T} is therefore based on the energy E_j measured in the calorimeter's jth tower,

$$E_{\mathrm{T}} = \sum_{j=1}^{M} E_j \sin \theta_j, \qquad (1)$$

where j runs over all M towers in the calorimeter and θ_j is the polar angle of the calorimeter tower. The transverse energy can also be calculated using single-particle tracks. In that case, the index j in Eq. (1) runs over the M measured particles instead of calorimeter towers and θ_{j} is the particle emission angle. To be compatible with the E_{T} of a calorimetry measurement, the energy E_{j} of Eq. (1) must be replaced with the single-particle

energies

$$E_j = \begin{cases} E_{kin} & \text{for baryons,} \\ E_{kin} + 2mc^2 & \text{for antibaryons,} \\ E_{kin} + mc^2 & \text{for all other particles.} \end{cases} \quad (2)$$

This definition of E_T was used in the measurements of the transverse energy by CMS [30] (based on calorimetry), PHENIX [26] (based on electromagnetic calorimetry), and STAR [29] (based on a combination of electromagnetic calorimetry and charged-particle tracking). To facilitate comparison between the various data sets the definition of E_T given by Eqs. (1) and (2) is used here.

It is useful to classify particles by how they interact with the detector. We define the following categories of final-state particles:

(A) $\pi^\pm$, $K^\pm$, p, and $\overline{p}$: Charged particles measured with high efficiency by tracking detectors

(B) π^0, ω, η, $e^\pm$, and γ, particles measured with high efficiency by electromagnetic calorimeters;

(C) Λ, $\overline{\Lambda}$, K_S^0, Σ^+, Σ^-, and Σ^0, particles measured with low efficiency in tracking detectors and electromagnetic calorimeters;

(D) K_L^0, n, and $\overline{n}$, neutral particles not measured well by either tracking detectors or electromagnetic calorimeters.

The total E_T is the sum of the E_T observed in final-state particles in categories A–D. Contributions from all other particles are negligible. In HIJING 1.383 [46] simulations of Pb-Pb collisions at $\sqrt{s_{NN}} = 2.76$ TeV the next-largest contributions come from the $\Xi(\overline{\Xi})$ and $\Omega(\overline{\Omega})$ baryons with a total contribution of about 0.4% of the total E_T, much less than the systematic uncertainty on the final value of E_T. The E_T from unstable particles with $c\tau < 1$ cm is taken into account through the E_T from their decay particles.

When measuring E_T using tracking detectors, the primary measurement is of particles in category A and corrections must be applied to take into account the E_T which is not observed from particles in categories B–D. In the hybrid method the E_T from particles in category A is measured using tracking detectors and the E_T from particles in category B is measured by the electromagnetic calorimeter. An electromagnetic calorimeter has the highest efficiency for measuring particles in category B, although there is a substantial background from particles in category A. The E_T from categories C and D, which is not well measured by an electromagnetic calorimeter, must be corrected for on average. Following the convention used by STAR, we define E_T^{had} to be the E_T measured from particles in category A and scaled up to include particles in categories C and D and E_T^{em} to be the E_T measured in category B. The total E_T is given by

$$E_T = E_T^{had} + E_T^{em}. \quad (3)$$

We refer to E_T^{had} as the hadronic E_T and E_T^{em} as the electromagnetic E_T. We note that E_T^{had} and E_T^{em} are operational definitions based on the best way to observe the energy deposited in various detectors and that the distinction is not theoretically meaningful.

TABLE I. Summary of corrections and systematic uncertainties for E_T^{had} and E_T from tracking detectors. For centrality- and p_T-independent corrections the correction is listed. For centrality- and p_T-dependent corrections, the approximate percentage of the correction is listed. In addition, the anchor-point uncertainty in the Glauber calculations leads to an uncertainty of 0%–4%, increasing with centrality.

Correction	Value	Relative uncertainty
$f_{p_{Tcut}}$	0.9710 ± 0.0058	0.6
$f_{neutral}$	0.728 ± 0.017	2.3
f_{total}	0.553 ± 0.010	3.0
f_{notID}	0.982 ± 0.002	0.2
$f_{bg}(p_T)$	1.8%	0.8
$\varepsilon(p_T)$	50%	5

Several corrections are calculated using HIJING [46] simulations. The propagation of final-state particles in these simulations through the ALICE detector material is described using GEANT3 [47]. Throughout the paper these are described as HIJING + GEANT simulations.

A. Tracking detector measurements of E_T

The measurements of the total E_T using the tracking detectors and of the hadronic E_T are closely correlated because the direct measurement in both cases is $E_T^{\pi,K,p}$, the E_T from $\pi^\pm$, $K^\pm$, p, and $\overline{p}$ from the primary vertex. All contributions from other categories are treated as background. For E_T^{had} the E_T from categories C and D is corrected for on average and for the total E_T the contribution from categories B, C, and D is corrected for on average. Each of these contributions is taken into account with a correction factor.

The relationship between the measured track momenta and $E_T^{\pi,K,p}$ is given by

$$\frac{dE_T^{\pi,K,p}}{d\eta} = \frac{1}{\Delta\eta} \frac{1}{f_{p_{Tcut}}} \frac{1}{f_{notID}} \sum_{i=1}^{n} \frac{f_{bg}(p_T^i)}{\varepsilon(p_T^i)} E_i \sin\theta_i \quad (4)$$

where i runs over the n reconstructed tracks and $\Delta\eta$ is the pseudorapidity range used in the analysis; $\varepsilon(p_T)$ corrects for the finite track reconstruction efficiency and acceptance, $f_{bg}(p_T)$ corrects for the Λ, $\overline{\Lambda}$, and K_S^0 daughters and electrons that pass the primary track quality cuts; f_{notID} corrects for particles that could not be identified unambiguously through their specific energy loss dE/dx in the TPC; and $f_{p_{Tcut}}$ corrects for the finite detector acceptance at low momentum. Hadronic E_T is given by $E_T^{had} = E_T^{\pi,K,p}/f_{neutral}$, where $f_{neutral}$ is the fraction of E_T^{had} from $\pi^\pm$, $K^\pm$, p, and $\overline{p}$ and total E_T is given by $E_T = E_T^{\pi,K,p}/f_{total}$ where f_{total} is the fraction of E_T from $\pi^\pm$, $K^\pm$, p, and $\overline{p}$. The determination of each of these corrections is given below and the systematic uncertainties are summarized in Table I. Systematic uncertainties are correlated point to point.

1. Single-track efficiency × acceptance $\varepsilon(p_T)$

The single-track efficiency × acceptance is determined by comparing the primary yields to the reconstructed yields using

HIJING + GEANT simulations, as described in Ref. [48]. When a particle can be identified as a $\pi^\pm$, $K^\pm$, p, or $\overline{p}$ using the algorithm described above, the efficiency for that particle is used. Otherwise the particle-averaged efficiency is used. The 5% systematic uncertainty is determined by the difference between the fraction of TPC stand-alone tracks matched with a hit in the ITS in simulations and data.

2. Background $f_{bg}(p_T)$

The background comes from photons which convert to e^+e^- in the detector and decay daughters from Λ, $\overline{\Lambda}$, and K_S^0, which are observed in the tracking detectors but do not originate from primary $\pi^\pm$, $K^\pm$, p, and $\overline{p}$. This is determined from HIJING + GEANT simulations. The systematic uncertainty on the background owing to conversion electrons is determined by varying the material budget in the HIJING + GEANT simulationsby $\pm 10\%$ and found to be negligible compared to other systematic uncertainties. The systematic uncertainty owing to Λ, $\overline{\Lambda}$, and K_S^0 daughters is sensitive to both the yield and the shape of the Λ, $\overline{\Lambda}$, and K_S^0 spectra. To determine the contribution from Λ, $\overline{\Lambda}$, and K_S^0 decay daughters and its systematic uncertainty, the spectra in simulation are reweighted to match the data and the yields are varied within their uncertainties [49]. Because the centrality dependence is less than the uncertainty owing to other corrections, a constant correction of 0.982 ± 0.008 is applied across all centralities.

3. Particle identification f_{notID}

The E_T of particles with $0.15 < p_T < 0.45$ GeV/c with a dE/dx within two standard deviations of the expected dE/dx for kaons is calculated using the kaon mass and the E_T of particles with $0.15 < p_T < 0.9$ GeV/c with a dE/dx within two standard deviations of the expected dE/dx for (anti)protons is calculated using the (anti)proton mass. The E_T of all other particles is calculated using the pion mass. Because the average transverse momentum is $\langle p_T \rangle = 0.678 \pm 0.007$ GeV/c for charged particles [50] and over 80% of the particles created in the collision are pions [45], most particles can be identified correctly using this algorithm. At high momentum, the difference between the true E_T and the E_T calculated using the pion mass hypothesis for kaons and protons is less than at low p_T. This is therefore a small correction. Assuming that all kaons with $0.15 < p_T < 0.45$ GeV/c and (anti)protons with $0.15 < p_T < 0.9$ GeV/c are identified correctly and using the identified $\pi^\pm$, $K^\pm$, p, and $\overline{p}$ spectra [45] gives $f_{notID} = 0.992 \pm 0.002$. The systematic uncertainty is determined from the uncertainties on the yields.

Assuming that 5% of kaons and protons identified using the particle-identification algorithm described above are misidentified as pions only decreases f_{notID} by 0.0002, less than the systematic uncertainty on f_{notID}. This indicates that this correction is robust to changes in the mean dE/dx expected for a given particle and its standard deviation. We note that either assuming no particle identification or doubling the number of kaons and protons only decreases f_{notID} by 0.005.

4. Low p_T acceptance $f_{p_{Tcut}}$

The lower momentum acceptance of the tracking detectors is primarily driven by the magnetic field and the inner radius of the active volume of the detector. Tracks can be reliably reconstructed in the TPC for particles with $p_T > 150$ MeV/c. The fraction of E_T carried by particles below this momentum cutoff is determined by HIJING + GEANT simulations. To calculate the systematic uncertainty, we follow the prescription given by STAR [29]. The fraction of E_T contained in particles below 150 MeV/c is calculated assuming that all particles below this cutoff have a momentum of exactly 150 MeV/c to determine an upper bound, assuming that they have a momentum of 0 MeV/c to determine a lower bound, and using the average as the nominal value. Using this prescription, $f_{p_{Tcut}} = 0.9710 \pm 0.0058$. We note that $f_{p_{Tcut}}$ is the same within systematic uncertainties when calculated from PYTHIA simulations [51] for pp collisions with $\sqrt{s} = 0.9$ and 8 TeV, indicating that this is a robust quantity.

5. Correction factors $f_{neutral}$ and f_{total}

Under the assumption that the different states within an isospin multiplet and particles and antiparticles have the same E_T, $f_{neutral}$ can be written as

$$f_{neutral} = \frac{2E_T^\pi + 2E_T^K + 2E_T^p}{3E_T^\pi + 4E_T^K + 4E_T^p + 2E_T^\Lambda + 6E_T^\Sigma} \qquad (5)$$

and f_{total} can be written as

$$f_{total} = \frac{2E_T^\pi + 2E_T^K + 2E_T^p}{3E_T^\pi + 4E_T^K + 4E_T^p + 2E_T^\Lambda + 6E_T^\Sigma + E_T^{\omega,\eta,e^\pm,\gamma}}. \qquad (6)$$

where E_T^K is the E_T from one kaon species, E_T^π is the E_T from one pion species, E_T^p is the average of the E_T from protons and antiprotons, E_T^Λ is the average E_T from Λ and $\overline{\Lambda}$, and E_T^Σ is the average E_T from Σ^+, Σ^-, and Σ^0 and their antiparticles. The contributions E_T^π, E_T^K, E_T^p, and E_T^Λ are calculated from the particle spectra measured by ALICE [45,49] as for the calculation of E_T from the particle spectra. The systematic uncertainties are also propagated assuming that the systematic uncertainties from different charges of the same particle species (e.g., π^+ and π^-) are 100% correlated and from different species (e.g., π^+ and K^+) are uncorrelated. The contribution from the Σ^+, Σ^-, and Σ^0 and their antiparticles is determined from the measured Λ spectra. The total contribution from Σ species and their antiparticles should be approximately equal to that of the Λ and $\overline{\Lambda}$, but because there are three isospin states for the Σ, each species carries roughly 1/3 of the E_T that the Λ carries. Because the Σ^0 decays dominantly through a Λ and has a short lifetime, the measured Λ spectra include Λ from the Σ^0 decay. The ratio of $F = (E_T^{\Sigma^+} + E_T^{\Sigma^-})/E_T^\Lambda$ is therefore expected to be 0.5. HIJING [46] simulations indicate that $F = 0.67$ and if the E_T scales with the yield, THERMUS [52] indicates that $F = 0.532$. We therefore use $F = 0.585 \pm 0.085$.

The contribution $E_T^{\omega,\eta,e^\pm,\gamma}$ is calculated using transverse mass scaling for the η meson and PYTHIA simulations for the

ω, $e^{\pm}$, and γ, as described earlier. Because most of the E_T is carried by $\pi^{\pm}$, $K^{\pm}$, p, $\overline{p}$, n, and $\overline{n}$, whose contributions appear in both the numerator and the denominator, f_{total} and $f_{neutral}$ can be determined to high precision, and the uncertainty in f_{total} and $f_{neutral}$ is driven by E_T^{Λ} and $E_T^{\omega,\eta,e^{\pm},\gamma}$. It is worth considering two special cases. If all E_T were carried by pions, as is the case at low energy where almost exclusively pions are produced, Eq. (6) would simplify to $f_{total} = 2/3$. If all E_T were only carried by kaons, (anti)protons, and (anti)neutrons, Eq. (6) would simplify to $f_{total} = 1/2$.

To calculate the contribution from the η meson and its uncertainties, we assume that the shapes of its spectra for all centrality bins as a function of transverse mass are the same as the pion spectra, using the transverse mass scaling [53], and that the η/π ratio is independent of the collision system, as observed by PHENIX [54]. We also consider a scenario where the η spectrum is assumed to have the same shape as the kaon spectrum, as would be expected if the shape of the η spectrum was determined by hydrodynamical flow. In this case we use the ALICE measurements of η/π in pp collisions [55] to determine the relative yields. We use the η/π ratio at the lowest momentum point available, $p_T = 0.5$ GeV/c, because the E_T measurement is dominated by low-momentum particles. Because no ω measurement exists, PYTHIA [51] simulations of pp collisions were used to determine the relative contribution from the ω and from all other particles which interact electromagnetically (mainly γ and $e^{\pm}$). These contributions were approximately 2% and 1% of E_T^{π}, respectively. With these assumptions, $E_T^{\omega,\eta,e^{\pm},\gamma}/E_T^{\pi} = 0.17 \pm 0.11$. The systematic uncertainty on this fraction is dominated by the uncertainty in the η/π ratio. We propagate the uncertainties assuming that the E_T from the same particle species are 100% correlated and that the uncertainties from different particle species are uncorrelated.

The $f_{neutral}$, f_{total}, and $f_{em} = 1 - f_{total}/f_{neutral}$ are shown in Fig. 1 along with the fractions of E_T carried by all pions f_{π}, all kaons f_K, protons and antiprotons f_p, and Λ baryons f_{Λ} versus $\langle N_{part} \rangle$. While there is a slight dependence of the central value on $\langle N_{part} \rangle$, this variation is less than the systematic uncertainty. Because there is little centrality dependence, we use $f_{em} = 0.240 \pm 0.027$, $f_{neutral} = 0.728 \pm 0.017$, and $f_{total} = 0.553 \pm 0.010$, which encompass the entire range for all centralities. The systematic uncertainty is largely driven by the contribution from Λ, ω, η, $e^{\pm}$, and γ because these particles only appear in the denominator of Eqs. (5) and (6). The systematic uncertainty on f_{total} is smaller than that on $f_{neutral}$ because $f_{neutral}$ only has E_T^{Λ} in the denominator.

These results are independently interesting. There is little change in the fraction of energy carried by different species with centrality and the changes are included in the f_{total} used for the measurement of E_T. Additionally, only about 1/4 of the energy is in E_T^{em}, much less than the roughly 1/3 of energy in E_T^{em} at lower energies, where most particles produced are pions with the π^0 carrying approximately 1/3 of the energy in the collision. Furthermore, only about 3.5% of the E_T is carried by ω, η, $e^{\pm}$, and γ. Because charged and neutral pions have comparable spectra, this means that the tracking detectors are highly effective for measuring the transverse energy distribution in nuclear collisions.
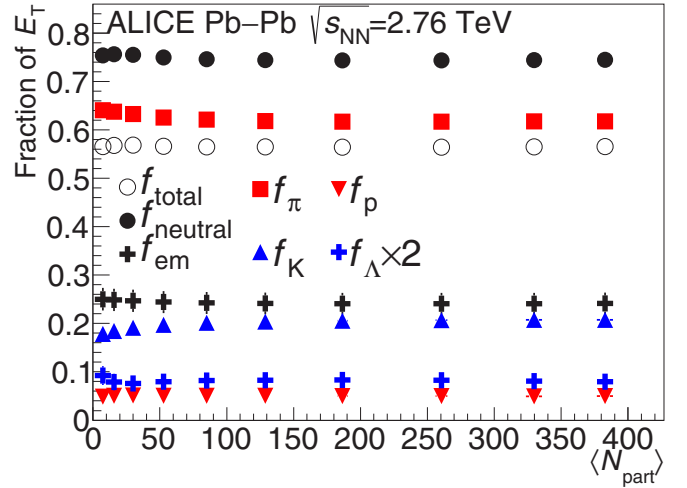

FIG. 1. Fraction of the total E_T in pions (f_{π}), kaons (f_K), p and $\overline{p}$ (f_p), and Λ (f_{Λ}) and the correction factors f_{total}, $f_{neutral}$, and f_{em} as functions of $\langle N_{part} \rangle$. The fraction f_{Λ} is scaled by a factor of two so that the data do not overlap with those from protons. Note that $f_{neutral}$ is the fraction of E_T^{had} measured in the tracking detectors, while f_{total} and f_{em} are the fractions of the total E_T measured in the tracking detectors and the calorimeters, respectively. The vertical error bars give the uncertainty on the fraction of E_T from the particle yields.

6. E_T^{had} distributions

Figure 2 shows the distributions of the reconstructed E_T^{had} measured from $\pi^{\pm}$, $K^{\pm}$, p, and $\overline{p}$ tracks using the method described above for several centralities. No correction was done for the resolution, leaving these distributions dominated by resolution effects. The mean E_T^{had} is determined from the average of the distribution of E_T^{had} in each centrality class.

B. Calculation of E_T and E_T^{had} from measured spectra

We use the transverse momentum distributions (spectra) measured by ALICE [45,49] to calculate E_T and E_T^{had} as a cross-check. We assume that all charge signs and isospin states
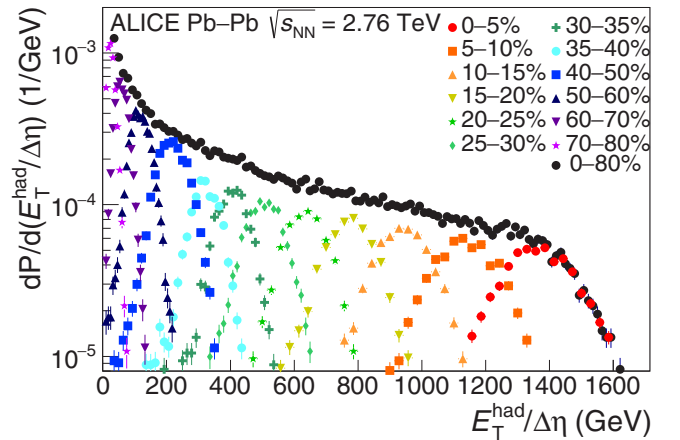

FIG. 2. Distribution of E_T^{had} measured from $\pi^{\pm}$, $K^{\pm}$, p, and $\overline{p}$ tracks at midrapidity for several centrality classes. Not corrected for resolution effects. Only statistical error bars are shown.
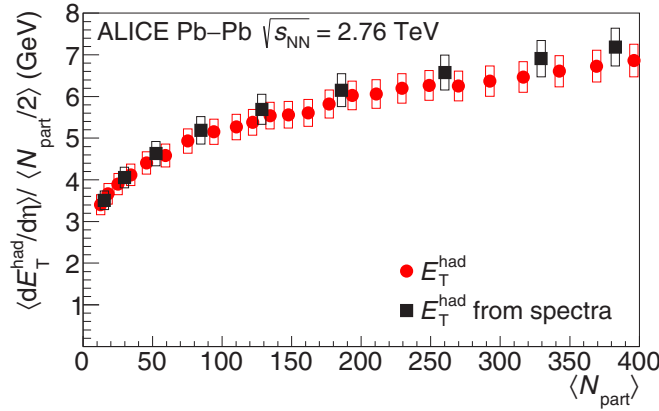
FIG. 3. Comparison of $\langle dE_T^{\text{had}}/d\eta \rangle/\langle N_{\text{part}}/2 \rangle$ versus $\langle N_{\text{part}} \rangle$ from the measured particle spectra and as calculated from the tracking detectors. The boxes indicate the systematic uncertainties.

of each particle carry the same E_T, e.g., $E_T^{\pi^+} = E_T^{\pi^-} = E_T^{\pi^0}$, and that the E_T carried by (anti)neutrons equals the E_T carried by (anti)protons. These assumptions are consistent with the data at high energies where positively and negatively charged hadrons are produced at similar rates and the antibaryon to baryon ratio is close to one [56,57]. Because the Λ spectra [49] are only measured for five centrality bins, the Λ contribution is interpolated from the neighboring centrality bins. The same assumptions about the contributions of the η, ω, γ, and $e^{\pm}$ described in the section on f_{total} and f_{neutral} are used for these calculations. The dominant systematic uncertainty on these measurements is attributable to the single track reconstruction efficiency and is correlated point to point. The systematic uncertainty on these calculations is not correlated with the calculations of E_T using the tracking detectors because these measurements are from data collected in different years. The mean E_T^{had} per $\langle N_{\text{part}}/2 \rangle$ obtained from the tracking results of Fig. 2 are shown as a function of $\langle N_{\text{part}} \rangle$ in Fig. 3, where they are compared with results calculated using the particle spectra measured by ALICE. The two methods give consistent results. Data are plotted in 2.5% wide bins in centrality for 0%–40% central collisions, where the uncertainty on the centrality is <1% [58]. Data for 40%–80% central collisions are plotted in 5% wide bins.

C. Electromagnetic calorimeter measurements of E_T^{em}

The E_T^{em} is defined as the transverse energy of the particles of category B discussed above, which are the particles measured well by an electromagnetic calorimeter. While the definition of E_T^{em} includes π^0, ω, η, $e^{\pm}$, and γ, the majority of the E_T comes from $\pi^0 \to \gamma\gamma$ (85%) and $\eta \to \gamma\gamma$ (12%) decays, meaning that the vast majority of E_T^{em} arises from photons reaching the active area of the electromagnetic calorimeters. Reconstructed clusters are used for the analysis, with most clusters arising from a single γ. Clusters reduce contributions from detector noise to a negligible level, as compared to using tower energies as done by STAR [29]. However, clusters also require additional corrections for the reconstruction efficiency, nonlinearity, and minimum energy

TABLE II. Summary of corrections and systematic uncertainties for E_T^{em}. The approximate size of the correction is listed for ε_γ and the ranges are listed for centrality dependent corrections. The fraction $f_{\text{bkgd}} = E_T^{\text{bkgd}}/E_T^{\text{raw}}$, where $E_T^{\text{raw}} = \sum_j \delta_m \frac{\sin \theta_j}{\varepsilon_\gamma f_{E_{\text{NL}}}} E_j$ is given to compare E_T^{bkgd} across centralities. In addition, the anchor-point uncertainty in the Glauber calculations leads to an uncertainty of 0%–4%, increasing with centrality.

	PHOS		EMCal	
	Correction	Uncertainty	Correction	Uncertainty
f_{acc}	6	0	3.6	0
Energy scale	–	0.5%	–	2%
ε_γ	40%	5%	80%	5%
$f_{E_{\text{Tmin}}}$	0.735–0.740	3.5%	0.64–0.673	4.1%–5.0%
$f_{E_{\text{NL}}}$	<0.5%	1.3%	<5%	0.8%
f_{bkgd}	0.616–0.753	9%–20%	0.659–0.732	8%–13%
E_T^{em}	–	10%–20%	–	10%–15%

reconstructed. In addition, both the EMCal and the PHOS have limited nominal acceptances so an acceptance correction must be applied. Backgrounds come from charged hadrons in category A ($\pi^{\pm}$, $K^{\pm}$, p, and $\overline{p}$), kaon decays into π^0 from both category A ($K^{\pm}$) and category C (K_S^0), neutrons from category D, and particles produced by secondary interactions with the detector material.

The corrected E_T^{em} is given by

$$\frac{dE_T^{\text{em}}}{d\eta} = \frac{1}{\Delta\eta} \frac{1}{f_{\text{acc}}} \frac{1}{f_{E_{\text{Tmin}}}} \left(\sum_j \delta_m \frac{\sin\theta_j}{\varepsilon_\gamma f_{E_{\text{NL}}}} E_j - E_T^{\text{bkgd}} \right), \quad (7)$$

where j runs over the reconstructed clusters in the calorimeter and $\Delta\eta$ is the pseudorapidity range used in the analysis. The correction factor f_{acc} corrects for the finite nominal azimuthal detector acceptance, $f_{E_{\text{Tmin}}}$ is a correction for the minimum cluster energy used in the analysis, δ_m is zero when a cluster is matched to a track and one otherwise, ε_γ is the product of the active acceptance and the reconstruction efficiency in the nominal acceptance of the detector, $f_{E_{\text{NL}}}$ is the correction for the nonlinear response of the calorimeter, and E_T^{bkgd} is the sum of the contributions from charged hadrons, kaons, neutrons, and particles created by secondary interactions. These correction factors are discussed below and their systematic uncertainties are summarized in Table II. All of the systematic uncertainties except for that owing to the background subtraction are correlated point to point. Systematic uncertainties on measurements of E_T^{em} from the EMCal and the PHOS and calculations of E_T^{em} from the spectra are not correlated. Systematic uncertainties on hybrid measurements are dominated by systematic uncertainties on E_T^{had} and are therefore dominantly correlated point to point and with the tracking detector measurements.

1. Acceptance correction f_{acc} and cluster reconstruction efficiency ε_γ

The correction for the acceptance is divided into two parts, the correction owing to the nominal acceptance of the detector

and the correction owing to limited acceptance within the nominal acceptance of the detector owing to dead regions and edge effects. To reduce edge effects, clusters in the PHOS are restricted to $|\eta| < 0.1$ and in the EMCal to $|\eta| < 0.6$. The correction f_{acc} accounts for the limited nominal acceptance in azimuth and is therefore 5/18 for the EMCal, which has a nominal acceptance of $100°$, and 1/6 for the PHOS, which has a nominal acceptance of $60°$. It does not correct for acceptance effects owing to dead regions in the detector or for noisy towers omitted from the analysis. This is accounted for by the cluster reconstruction efficiency × acceptance within the nominal detector acceptance, ε_γ, calculated from HIJING + GEANT simulationsusing photons from the decay of the π^0 meson. The efficiency is calculated as a function of the energy of the cluster.

2. Minimum cluster energy $f_{E_{\text{Tmin}}}$

There is a minimum energy for usable clusters analogous to the minimum p_T in the acceptance of the tracking detectors. Thresholds of 250 MeV for PHOS and 300 MeV for the EMCal are applied. These energies are above the peak energy for minimum ionizing particles (MIPs), reducing the background correction owing to charged hadrons. We apply the threshold in E_T rather than energy because it simplifies the calculation of the correction for this threshold and its systematic uncertainty. We use the charged pion spectra to calculate the fraction of E_T^{em} below these thresholds. PYTHIAis used to simulate the decay kinematics and the measured charged pion spectra are used to determine the fraction of E_T from pions within the acceptance. As for the calculation of f_{total} for the measurement of E_T^{had} described above, we assume transverse mass scaling to determine the shape of the η spectrum and the η/π ratio measured by ALICE [55] to estimate the contribution of the η meson to $f_{E_{\text{Tmin}}}$. The uncertainty on the shape of the charged pion spectrum and on the η/π ratio is used to determine the uncertainty on $f_{E_{\text{Tmin}}}$. This correction is centrality dependent and ranges from 0.735 to 0.740 for the PHOS and from 0.640 to 0.673 for the EMCal with a systematic uncertainty of 3.5%–5%.

3. Nonlinearity correction $f_{E_{\text{NL}}}$ and energy scale uncertainty

For an ideal calorimeter the signal observed is proportional to the energy. In practice, however, there is a slight deviation from linearity in the signal observed, particularly at low energies. A nonlinearity correction is applied to take this into account. For the EMCal this deviation from linearity reaches a maximum of about 15% for the lowest energy clusters used in this analysis. The systematic uncertainty for the EMCal is determined by comparing the nonlinearity observed in test beam and the nonlinearity predicted by HIJING + GEANT simulationsand reaches a maximum of about 5% for the lowest energy clusters. The PHOS nonlinearity is determined by comparing the location of the π^0 mass peak to HIJING + GEANT simulationsand cross checked using the energy divided by the momentum for identified electrons. The systematic uncertainty is derived from the accuracy of the location of the π^0 mass peak. The nominal correction is about 1% with a maximum systematic uncertainty of

around 3% for the lowest energy clusters. The raw E_T^{em} is calculated with the maxima and minima of the nonlinearities and the difference from the nominal value is assigned as a systematic uncertainty. The final systematic uncertainty on the measurement with the EMCal owing to nonlinearity is about 0.8% and 1.3% for the PHOS. For both the PHOS and the EMCal, the energy scale uncertainty was determined by comparing the location of the π^0 mass peak and the ratio of energy over momentum for electrons. This systematic uncertainty is 2% for the EMCal [59] and 0.5% for the PHOS [60].

4. Background E_T^{bkgd}

Charged particles (category A) are the largest source of background in E_T^{em}. Clusters matched to tracks are omitted from the analysis. The track matching efficiency determined from HIJING + GEANT simulationsis combined with information from clusters matched to tracks to calculate the number and mean energy of remaining deposits from charged particles. The systematic uncertainty on this contribution comes from the uncertainty on the track matching efficiency and the uncertainty in the mean energy. The former is dominated by the uncertainty on the single-track reconstruction efficiency and the latter is determined by comparing central and peripheral collisions, assuming that the energy of clusters matched to tracks in central collisions may be skewed by overlapping clusters owing to the high occupancy.

The background contributions from both charged kaons (category A) through their $K^\pm \to X\pi^0$ decays and K_S^0 (category C) through its $K_S^0 \to \pi^0\pi^0$ decay are non-negligible. The amount of energy deposited by a kaon as a function of p_T is determined using HIJING + GEANT simulations. This is combined with the kaon spectra measured by ALICE [45] to calculate the energy deposited in the calorimeters by kaons. The systematic uncertainty on the background from kaons is determined by varying the yields within the uncertainties of the spectra. Contributions from both neutrons and particles from secondary interactions are determined using HIJING + GEANT simulations. The systematic uncertainty on these contributions is determined by assuming that they scale with either the number of tracks (as a proxy for the number of charged particles) or with the number of calorimeter clusters (as a proxy for the number of neutral particles).

The background contribution is centrality dependent and ranges from 61% to 73% with both the background and its systematic uncertainty dominated by contributions from charged hadrons. This correction is so large because E_T^{em} comprises only about 25% of the E_T in an event while $\pi^\pm$, $K^\pm$, p, and $\overline{p}$ carry roughly 57% of the E_T in an event.

5. Acceptance effects

The limited calorimeter acceptance distorts the distribution of E_T^{em} for events with very low E_T^{em} because it is difficult to measure the mean E_T when the mean number of clusters observed is small (about 1–10). While it is possible to correct for acceptance, this was not done because the measurement of E_T from the tracking method has the highest precision. The hybrid method using both the calorimeters and the tracking
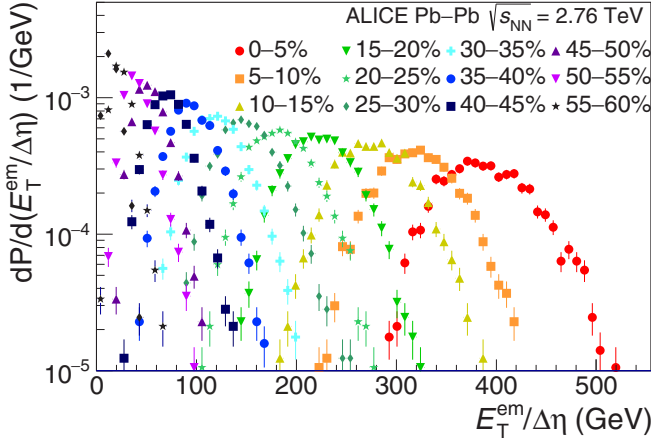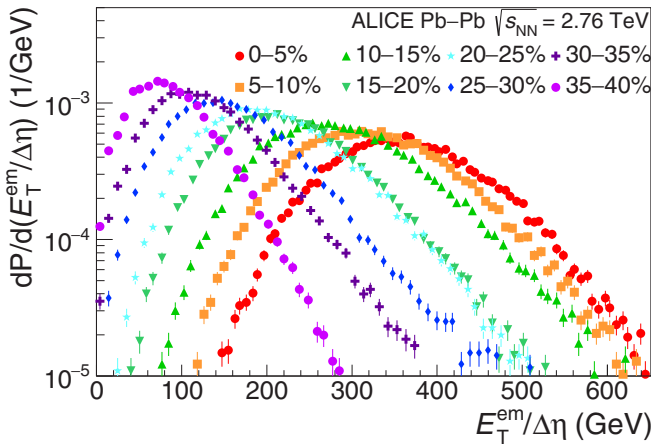
FIG. 4. Distribution of E_T^{em} measured with the EMCal at midrapidity for several centrality bins. Not corrected for resolution effects. Only statistical error bars are shown.
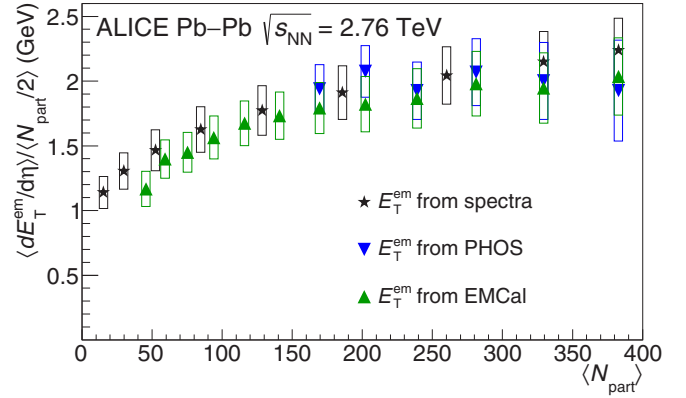
detectors is therefore restricted to the most central collisions where distortions of the E_T^{em} distribution are negligible.

6. E_T^{em} distributions

Figure 4 shows the distributions of the reconstructed E_T^{em} measured using the EMCal and Fig. 5 shows the distributions of the reconstructed E_T^{em} measured using the PHOS. No resolution correction was applied for the resolution leaving the distributions in Figs. 4 and 5 dominated by resolution effects. The resolution is primarily determined by the finite acceptance of the detectors in azimuth, limiting the fraction of E_T^{em} sampled by the calorimeter. The distributions are broader for PHOS than EMCal because of the smaller azimuthal acceptance of the PHOS. The mean E_T^{em} is determined from the average of the distribution of E_T^{em} in each centrality bin. The E_T^{em} per $\langle N_{part} \rangle$ pair measured using the electromagnetic calorimeters is compared to that calculated using the measured pion spectra in Fig. 6, demonstrating that these methods

FIG. 6. Comparison of $\langle dE_T^{em}/d\eta \rangle / \langle N_{part}/2 \rangle$ versus $\langle N_{part} \rangle$ at midrapidity from the PHOS, from the EMCal, and as calculated from the measured pion spectra. The boxes indicate the systematic uncertainties.

lead to comparable results. The E_T^{em} calculated from the spectra is determined using the same ratio of $E_T^{\omega, \eta, e^{\pm}, \gamma} / E_T^{\pi} = 0.171 \pm 0.110$ for all centralities.

IV. RESULTS

The $\langle dE_T/d\eta \rangle / \langle N_{part}/2 \rangle$ versus $\langle N_{part} \rangle$ is shown in Fig. 7 using tracking detectors, using EMCal + tracking, using PHOS + tracking, and as calculated from the measured particle spectra. All methods lead to comparable results, although the systematic errors are largely correlated owing to the dominant correction from the tracking inefficiency. The determination of $\langle N_{part} \rangle$ and its uncertainties are calculated using a Glauber model as in Refs. [58,61] and the uncertainties on $\langle N_{part} \rangle$ are added in quadrature to the uncertainties on E_T.

As discussed above, the small number of clusters observed in the calorimeters in peripheral collisions make acceptance corrections difficult. Because the measurements with the tracking detectors alone have higher precision, only these measurements are used in the following.
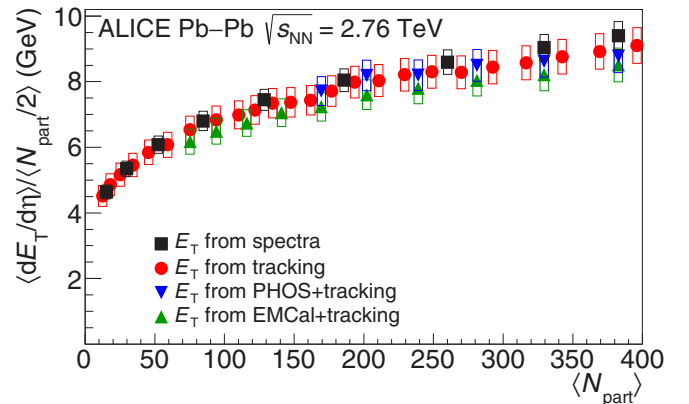

FIG. 5. Distribution of E_T^{em} measured with the PHOS at midrapidity for several centrality bins. Not corrected for resolution effects. Only statistical error bars are shown.

FIG. 7. Comparison of total $\langle dE_T/d\eta \rangle / \langle N_{part}/2 \rangle$ versus $\langle N_{part} \rangle$ at midrapidity using tracking detectors, using EMCal + tracking, using PHOS + tracking, and as calculated from the measured particle spectra. The boxes indicate the systematic uncertainties.
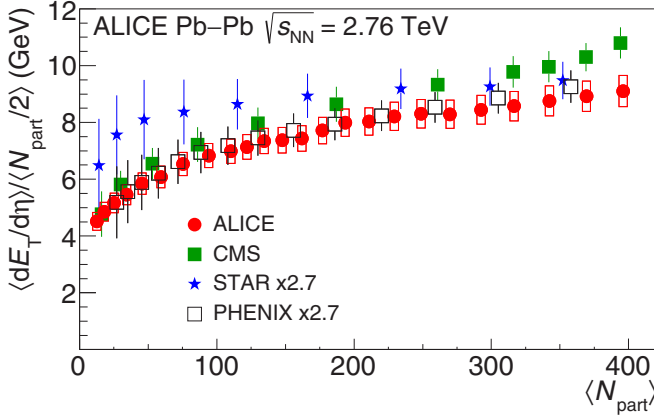
FIG. 8. Comparison of $\langle dE_T/d\eta\rangle/\langle N_{part}/2\rangle$ at midrapidity in Pb-Pb collisions at $\sqrt{s_{NN}} = 2.76$ TeV from CMS [30] and ALICE and in Au-Au collisions at $\sqrt{s_{NN}} = 200$ GeV from STAR [29] and PHENIX [26,27]. Data from RHIC were scaled by a factor of 2.7 for comparison of the shapes. The boxes indicate the systematic uncertainties.

Figure 8 compares $\langle dE_T/d\eta\rangle/\langle N_{part}/2\rangle$ versus $\langle N_{part}\rangle$ in Pb-Pb collisions at $\sqrt{s_{NN}} = 2.76$ TeV from CMS [30] and ALICE, and in Au-Au collisions at $\sqrt{s_{NN}} = 200$ GeV from STAR [29] and PHENIX [26,27]. Data from RHIC have been scaled by a factor of 2.7 for comparison of the shapes. The factor of 2.7 is approximately the ratio of $\langle p_T\rangle\langle dN_{ch}/d\eta\rangle$ at the LHC [45] to that at RHIC [62,63]. The shapes observed by ALICE and PHENIX are comparable for all $\langle N_{part}\rangle$. STAR measurements are consistent with PHENIX measurements for the most central collisions and above the PHENIX measurements, although consistent within systematic uncertainties, for more peripheral collisions. CMS measurements are consistent with ALICE measurements for peripheral collisions but deviate beyond the systematic uncertainties for more central collisions. The E_T in 0%–5% Pb-Pb collisions is $1737 \pm 6\text{(stat.)} \pm 97\text{(sys.)}$ GeV and the E_T per participant is $9.02 \pm 0.03\text{(stat.)} \pm 0.50\text{(sys.)}$ GeV, two standard deviations below the value observed by CMS [30]. All methods resulted in a lower E_T than that reported by CMS, although the systematic errors on the measurements are significantly correlated. One possible explanation of the differences is that the corrections for the CMS calorimetry measurement are determined by Monte Carlo [30], while the corrections for the ALICE measurement are mainly data driven.

PHENIX [28] reported that while $\langle dE_T/d\eta\rangle$ scaled by $\langle N_{part}\rangle$ has a pronounced centrality dependence, as seen in Fig. 8, $\langle dE_T/d\eta\rangle$ scaled by the number of constituent quarks, $\langle N_{quark}\rangle$, $\langle dE_T/d\eta\rangle/\langle N_{quark}/2\rangle$ shows little centrality dependence within the systematic uncertainties for collisions at $\sqrt{s_{NN}} = 62.4$–200 GeV. This indicates that E_T might scale linearly with the number of quarks participating in the collision rather than the number of participating nucleons. Figure 9 shows $\langle dE_T/d\eta\rangle/\langle N_{quark}/2\rangle$ as a function of $\langle N_{part}\rangle$. To calculate $\langle N_{quark}\rangle$ the standard Monte Carlo Glauber technique [32] has been used with the following Woods-Saxon nuclear density parameters: radius parameter $R_{WS} = 6.62 \pm 0.06$ fm, diffuseness $a = 0.546 \pm 0.010$ fm, and hard core
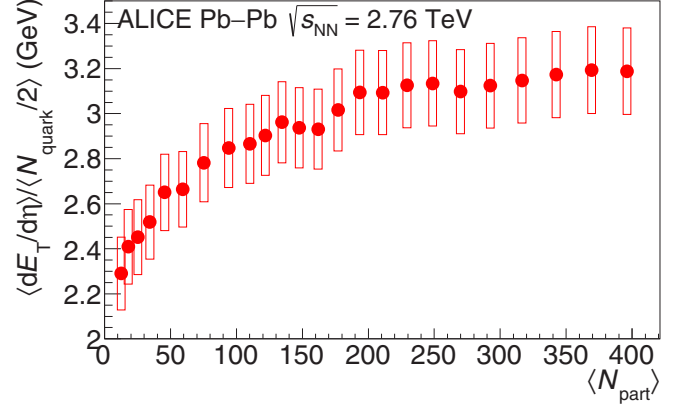

FIG. 9. Measurements of $\langle dE_T/d\eta\rangle/\langle N_{quark}/2\rangle$ versus $\langle N_{part}\rangle$ at midrapidity in Pb-Pb collisions at $\sqrt{s_{NN}} = 2.76$ TeV. Note the suppressed zero. The boxes indicate the systematic uncertainties.

$d_{min} = 0.4 \pm 0.4$ fm. The three constituent quarks in each nucleon have been sampled from the nucleon density distribution $\rho_{nucleon} = \rho_0 e^{-ar}$ with $a = 4.28$ fm^{-1} using the method developed by PHENIX [64]. The inelastic quark-quark cross section at $\sqrt{s_{NN}} = 2.76$ TeV was found to be $\sigma_{qq}^{inel} = 15.5 \pm 2.0$ mb, corresponding to $\sigma_{NN}^{inel} = 64 \pm 5$ mb [58]. The systematic uncertainties on the $\langle N_{quark}\rangle$ calculations were determined following the procedure described in Refs. [58,61]. Unlike at RHIC, we observe an increase in $\langle dE_T/d\eta\rangle/\langle N_{quark}/2\rangle$ with centrality below $\langle N_{part}\rangle \approx 200$.

Figure 10 shows $\langle dE_T/d\eta\rangle/\langle dN_{ch}/d\eta\rangle$, a measure of the average transverse energy per particle, versus $\langle N_{part}\rangle$ in Pb-Pb collisions at $\sqrt{s_{NN}} = 2.76$ TeV from ALICE and in Au-Au collisions at $\sqrt{s_{NN}} = 200$ GeV from STAR [29] and PHENIX [26,27]. No centrality dependence is observed within uncertainties at either RHIC or LHC energies. The $\langle dE_T/d\eta\rangle/\langle dN_{ch}/d\eta\rangle$ increases by a factor of approximately 1.25 from $\sqrt{s_{NN}} = 200$ GeV [26,27,29] to $\sqrt{s_{NN}} = 2.76$ TeV. This is comparable to the increase in $\langle p_T\rangle$ from $\sqrt{s_{NN}} = 200$ GeV to $\sqrt{s_{NN}} = 2.76$ TeV, which also shows little dependence
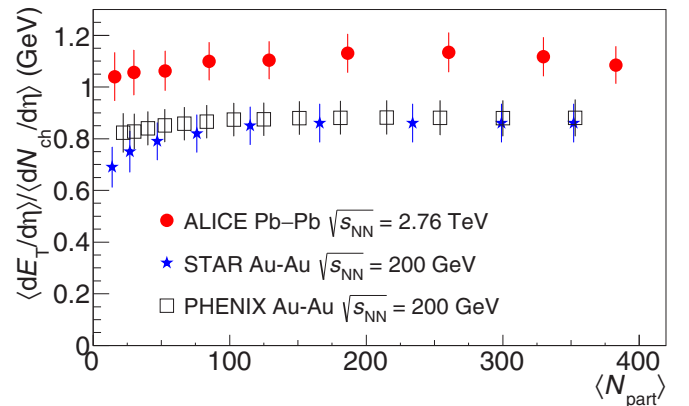

FIG. 10. Comparison of $\langle dE_T/d\eta\rangle/\langle dN_{ch}/d\eta\rangle$ versus $\langle N_{part}\rangle$ at midrapidity in Pb-Pb collisions at $\sqrt{s_{NN}} = 2.76$ TeV from ALICE and in Au-Au collisions at $\sqrt{s_{NN}} = 200$ GeV from STAR [29] and PHENIX [26,27].
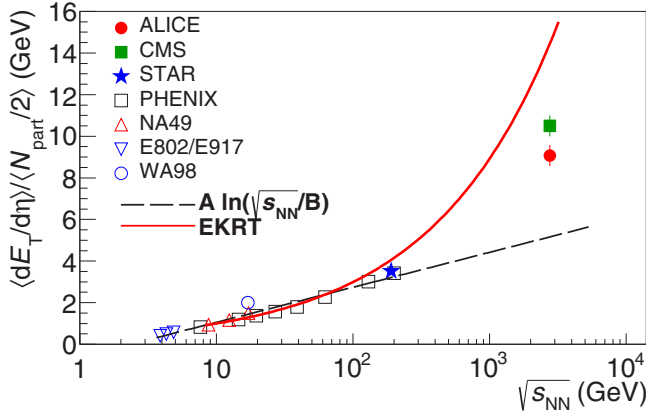
FIG. 11. Comparison of $\langle dE_T/d\eta\rangle/\langle N_{part}/2\rangle$ at midrapidity versus $\sqrt{s_{NN}}$ in 0%–5% central Pb-Pb collisions at $\sqrt{s_{NN}} = 2.76$ TeV from ALICE and CMS [30] and central collisions at other energies [26,29,64] at midrapidity. All measurements are from 0%–5% central collisions except the NA49 data, which are from 0%–7% collisions.

FIG. 12. Comparison of $\langle dE_T/d\eta\rangle/\langle dN_{ch}/d\eta\rangle$ at midrapidity versus $\sqrt{s_{NN}}$ in Pb-Pb collisions at $\sqrt{s_{NN}} = 2.76$ TeV from ALICE and measurements at other energies [19,23,25,26,29,64,67]. The band shows the extrapolation from lower energies with the width representing the uncertainty on the fit [26].

on the charged-particle multiplicity except in peripheral collisions [50]. The absence of a strong centrality dependence is consistent with the development of radial flow seen in the spectra of identified particles [50], where the kinetic energy is conserved during the hydrodynamic expansion instead of producing a higher $\langle p_T\rangle$.

Figure 11 shows a comparison of $\langle dE_T/d\eta\rangle/\langle N_{part}/2\rangle$ versus $\sqrt{s_{NN}}$ in 0%–5% central Pb-Pb collisions at $\sqrt{s_{NN}} = 2.76$ TeV from ALICE and CMS [30] and central collisions at other energies [26,29,64] at midrapidity. The data are compared to an extrapolation from lower energy data [26], which substantially underestimates the $\langle dE_T/d\eta\rangle/\langle N_{part}/2\rangle$ at the LHC. The data are also compared to the EKRT model [65,66]. The EKRT model combines perturbative QCD minijet production with gluon saturation and hydrodynamics. The EKRT calculation qualitatively describes the $\sqrt{s_{NN}}$ dependence at RHIC and SPS energies [29]. However, at LHC energies EKRT overestimates E_T substantially, indicating that it is unable to describe the collision energy dependence.

Figure 12 shows a comparison of $\langle dE_T/d\eta\rangle/\langle dN_{ch}/d\eta\rangle$ versus $\sqrt{s_{NN}}$ in 0%–5% central Pb-Pb collisions at $\sqrt{s_{NN}} = 2.76$ TeV from ALICE and in central collisions at other energies. Previous measurements indicated that $\langle dE_T/d\eta\rangle/\langle dN_{ch}/d\eta\rangle$ had either saturated at RHIC energies or showed only a weak dependence on $\sqrt{s_{NN}}$ [26,29,64]. An empirical extrapolation of the data to LHC energies assuming that both E_T and $\langle N_{ch}\rangle$ have a linear dependence on $\sqrt{s_{NN}}$ predicted that $\langle dE_T/d\eta\rangle/\langle dN_{ch}/d\eta\rangle$ would be 0.92 ± 0.06 [26] and we observe 1.06 ± 0.05. Increasing the incident energy increases both the particle production and the mean energy per particle at LHC energies, in contrast to lower energies ($\sqrt{s_{NN}} = 19.6$–200 GeV) where increasing the incident energy only led to increased particle production [26].

Figure 13 shows a comparison of $\langle dE_T/d\eta\rangle/\langle N_{part}/2\rangle$ versus $\langle N_{part}\rangle$ to various models. AMPT [68] is a Monte Carlo event generator that builds on HIJING [46], adding explicit interactions between initial minijet partons and final-state hadronic interactions. HYDJET 1.8 [69] is a Monte Carlo
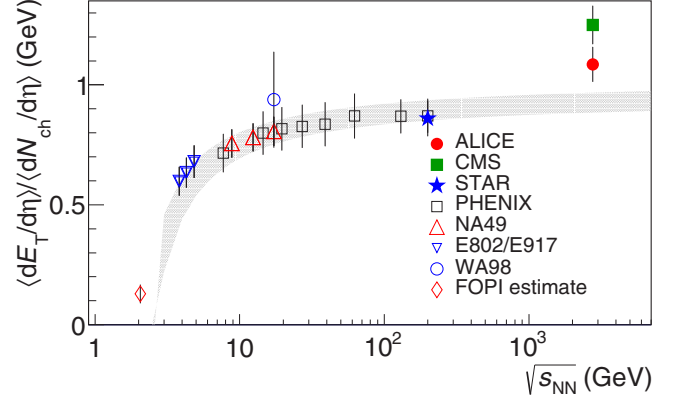
event generator that introduces jet quenching via gluon bremsstrahlung to PYTHIA [51] events. The HYDJET values use the E_T from HYDJET and the $\langle N_{part}\rangle$ from ALICE, similar to comparisons to HYDJET by CMS [30]. The curves labeled UDG are calculations from a color glass condensate model [70] with different normalization K factors. None of the available models is able to describe the data very well, but we find that AMPT does best in describing the shape and level of $\langle dE_T/d\eta\rangle/\langle N_{part}/2\rangle$. HYDJET describes the relative shape changes as a function of centrality as well as AMPT, but overestimates $\langle dE_T/d\eta\rangle/\langle N_{part}/2\rangle$. Both CGC calculations overestimate $\langle dE_T/d\eta\rangle/\langle N_{part}/2\rangle$ and predict a larger increase as a function of centrality than is observed in the data.

The volume-averaged energy density ε can be estimated from $\langle dE_T/d\eta\rangle$ using the expression [18]

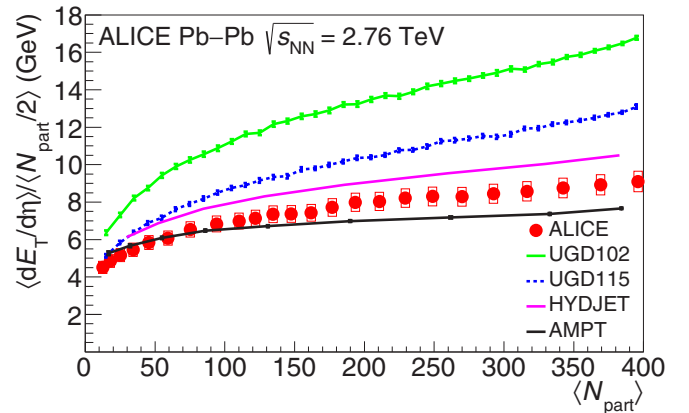$$\varepsilon = \frac{1}{Ac\tau_0} J\left\langle\frac{dE_T}{d\eta}\right\rangle, \qquad (8)$$

FIG. 13. Comparison of $\langle dE_T/d\eta\rangle/\langle N_{part}/2\rangle$ versus $\langle N_{part}\rangle$ at midrapidity to AMPT [68], HYDJET 1.8 [69], and UDG [70]. The boxes indicate the systematic uncertainties.
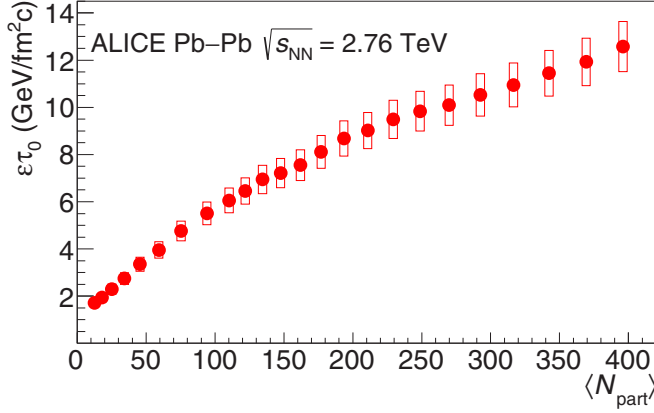
FIG. 14. $\varepsilon\tau_0$ versus $\langle N_{\text{part}}\rangle$ estimated using Eq. (8), $R = 7.17$ fm, and the measured $\langle dE_{\text{T}}/d\eta\rangle$. The boxes indicate the systematic uncertainties.

where A is the effective transverse collision area, c is the speed of light, J is the Jacobian for the transformation between $\langle dE_{\text{T}}/d\eta\rangle$ and $\langle dE_{\text{T}}/dy\rangle$, and τ_0 is the formation time. The Jacobian is calculated from the measured particle spectra [45,49]. While J has a slight centrality dependence, it is smaller than the systematic uncertainty so a constant Jacobian of $J = 1.12 \pm 0.06$ is used. The formation time of the system τ_0 is highly model dependent and we therefore report $\varepsilon\tau_0$.

The transverse overlap area corresponding to the measured $\langle dE_{\text{T}}/d\eta\rangle$ was determined by a calculation using a Glauber Monte Carlo method. Using the Glauber parameters from Ref. [58] and assuming each participating nucleon has an effective transverse radius of $R = (\sigma_{NN}^{\text{inel}}/4\pi)^{1/2} = 0.71$ fm results in $A = 162.5$ fm^2 for central collisions ($b = 0$ fm). This is equivalent to a transverse overlap radius of $R = 7.19$ fm, which is close to the value of 7.17 fm often used in estimates of energy densities using a Woods-Saxon distribution to determine the effective area [28,64]. The centrality dependence of A is obtained by assuming it scales as $(\sigma_x^2\sigma_y^2 - \sigma_{xy}^2)^{1/2}$ [71], where σ_x^2 and σ_y^2 are the variances and σ_{xy}^2 is the covariance of the spatial distribution of the participating nucleons in the transverse plane in the Glauber Monte Carlo calculation. For 0%–5% central collisions this leads to a reduction of A by 3%, resulting in $\varepsilon\tau_0 = 12.5 \pm 1.0$ GeV/fm^2/c. For comparison, using $R = 7.17$ fm gives $\varepsilon\tau_0 = 12.3 \pm 1.0$ GeV/fm^2/c, roughly 2.3 times that observed in 0%–5% central Au-Au collisions at $\sqrt{s_{NN}} = 200$ GeV. Some of this increase comes from the higher $\langle N_{\text{part}}\rangle$ in central Pb-Pb collisions relative to central Au-Au collisions. The energy density times the formation time $\varepsilon\tau_0$ is shown in Fig. 14 for $R = 7.17$ fm, the same value of R used by PHENIX at RHIC energies [28,64].

In addition to estimating the volume-averaged energy density, it is also interesting to estimate the energy density attained at the core of the collision area. This can be done by rewriting the Bjorken Eq. (8) as

$$\varepsilon_{\text{c}}\tau_0 = \frac{J}{c}\frac{\left\langle\frac{dE_{\text{T}}}{d\eta}\right\rangle_{\text{c}}}{A_{\text{c}}} = \frac{J}{c}\frac{\left\langle\frac{dE_{\text{T}}}{d\eta}\right\rangle}{\langle N_{\text{part}}\rangle}\sigma_{\text{c}}, \tag{9}$$

where A_{c} is the area of the transverse core, $\langle\frac{dE_{\text{T}}}{d\eta}\rangle_{\text{c}}$ is $\langle\frac{dE_{\text{T}}}{d\eta}\rangle$ produced in the core, and $\sigma_{\text{c}} = \langle N_{\text{part}}\rangle_{\text{c}}/A_{\text{c}}$ is the transverse area density of nucleon participants at the core. The area A_{c} was chosen arbitrarily to be a circle with a radius of 1 fm at the center of the collision. Equation (9) assumes that the local energy density scales with the participant density in the transverse plane and that the measured value of $\langle\frac{dE_{\text{T}}}{d\eta}\rangle/\langle N_{\text{part}}\rangle$, which is averaged over the total transverse collision area, is also representative of the transverse energy production at the core, $\langle\frac{dE_{\text{T}}}{d\eta}\rangle_{\text{c}}/\langle N_{\text{part}}\rangle_{\text{c}}$. The increase of this quantity with increasing centrality indicates that this is a conservative estimate. From a Glauber Monte Carlo calculation we find for 0%–5% centrality $\sigma_{\text{c}} = 4.2 \pm 0.1$ nucleon/fm^2, resulting in a core energy density of $\varepsilon_{\text{c}}\tau_0 = 21 \pm 2$ GeV/fm^2/c. For the most central 80 fm^2 (half the total overlap area) the energy density is still above 80% of the core energy density, emphasizing that the core energy density may be more relevant for judging the initial conditions of the QGP than the volume-averaged energy density.

V. CONCLUSIONS

We have measured $\langle dE_{\text{T}}/d\eta\rangle$ at midrapidity in Pb-Pb collisions at $\sqrt{s_{NN}} = 2.76$ TeV using four different methods. All methods lead to comparable results, although the systematic uncertainties are largely correlated. Our results are consistent with results from CMS [30] for 10%–80% central collisions; however, we observe a lower $\langle dE_{\text{T}}/d\eta\rangle$ in 0%–10% central collisions. The $\langle dE_{\text{T}}/d\eta\rangle$ observed at $\sqrt{s_{NN}} = 2.76$ TeV in 0%–5% central collisions is $1737 \pm 6(\text{stat.}) \pm 97(\text{sys.})$ GeV. The shape of the centrality dependence of $\langle dE_{\text{T}}/d\eta\rangle/\langle N_{\text{part}}/2\rangle$ is similar for RHIC and the LHC. No centrality dependence of $\langle dE_{\text{T}}/d\eta\rangle/\langle dN_{\text{ch}}/d\eta\rangle$ is observed within uncertainties, as was observed at RHIC. Unlike at RHIC, we observe an increase in $\langle dE_{\text{T}}/d\eta\rangle/\langle N_{\text{quark}}/2\rangle$ with centrality below $\langle N_{\text{part}}\rangle \approx 200$. Both $\langle dE_{\text{T}}/d\eta\rangle/\langle N_{\text{part}}/2\rangle$ and $\langle dE_{\text{T}}/d\eta\rangle/\langle dN_{\text{ch}}/d\eta\rangle$ in central collisions exceed the value expected from naive extrapolations from data at lower collision energies. Assuming that the formation time τ_0 is 1 fm/c the energy density is estimated to be at least 12.3 ± 1.0 GeV/fm^3 in 0%–5% central Pb-Pb collisions at $\sqrt{s_{NN}} = 2.76$ TeV and the energy density at the core of the collision exceeds 21 ± 2 GeV/fm^3.

[1] F. Karsch, Lattice QCD at high temperature and density, in *Lectures on Quark Matter*, edited by W. Plessas and L. Mathelitsch, Vol. 583 (Springer, Berlin, Heidelberg, 2002), pp. 209–249.

[2] A. Bazavov *et al.* (HotQCD Collaboration), Equation of state in (2+1)-flavor QCD, Phys. Rev. D **90**, 094503 (2014).

[3] K. Adcox *et al.* (PHENIX Collaboration), Formation of dense partonic matter in relativistic nucleus nucleus collisions at RHIC: Experimental evaluation by the PHENIX collaboration, Nucl. Phys. A **757**, 184 (2005).

[4] J. Adams *et al.* (STAR Collaboration), Experimental and theoretical challenges in the search for the quark gluon plasma: The STAR collaboration's critical assessment of the evidence from RHIC collisions, Nucl. Phys. A **757**, 102 (2005).

[5] B. B. Back *et al.* (PHOBOS Collaboration), The PHOBOS perspective on discoveries at RHIC, Nucl. Phys. A **757**, 28 (2005).

[6] I. Arsene *et al.* (BRAHMS Collaboration), Quark gluon plasma and color glass condensate at RHIC? The perspective from the BRAHMS experiment, Nucl. Phys. A **757**, 1 (2005).

[7] K. Aamodt *et al.* (ALICE Collaboration), Two-pion Bose-Einstein correlations in central Pb-Pb collisions at $\sqrt{s_{NN}} = 2.76$ TeV, Phys. Lett. B **696**, 328 (2011).

[8] K. Aamodt *et al.* (ALICE Collaboration), Centrality Dependence of the Charged-Particle Multiplicity Density at Mid-Rapidity in Pb-Pb Collisions at $\sqrt{s_{NN}} = 2.76$ TeV, Phys. Rev. Lett. **106**, 032301 (2011).

[9] K. Aamodt *et al.* (ALICE Collaboration), Suppression of charged particle production at large transverse momentum in central Pb-Pb collisions at $\sqrt{s_{NN}} = 2.76$ TeV, Phys. Lett. B **696**, 30 (2011).

[10] K. Aamodt *et al.* (ALICE Collaboration), Charged-Particle Multiplicity Density at Mid-Rapidity in Central Pb-Pb Collisions at $\sqrt{s_{NN}} = 2.76$ TeV, Phys. Rev. Lett. **105**, 252301 (2010).

[11] K. Aamodt *et al.* (ALICE Collaboration), Elliptic Flow of Charged Particles in Pb-Pb Collisions at 2.76 TeV, Phys. Rev. Lett. **105**, 252302 (2010).

[12] G. Aad *et al.* (ATLAS Collaboration), Observation of a Centrality-Dependent Dijet Asymmetry in Lead-Lead Collisions at $\sqrt{s_{NN}} = 2.76$ TeV with the ATLAS Detector at the LHC, Phys. Rev. Lett. **105**, 252303 (2010).

[13] S. Chatrchyan *et al.* (CMS Collaboration), Observation and studies of jet quenching in PbPb collisions at nucleon-nucleon center-of-mass energy $\sqrt{s_{NN}} = 2.76$ TeV, Phys. Rev. C **84**, 024906 (2011).

[14] S. Chatrchyan *et al.* (CMS Collaboration), Dependence on pseudorapidity and centrality of charged hadron production in PbPb collisions at a nucleon-nucleon center-of-mass energy of $\sqrt{s_{NN}} = 2.76$ TeV, J. High Energy Phys. 08 (2011) 141.

[15] S. Chatrchyan *et al.* (CMS Collaboration), Measurement of the elliptic anisotropy of charged particles produced in PbPb collisions at $\sqrt{s_{NN}} = 2.76$ TeV, Phys. Rev. C **87**, 014902 (2013).

[16] G. Aad *et al.* (ATLAS Collaboration), Measurement of the centrality dependence of the charged particle pseudorapidity distribution in lead-lead collisions at $\sqrt{s_{NN}} = 2.76$ TeV with the ATLAS detector, Phys. Lett. B **710**, 363 (2012).

[17] G. Aad *et al.* (ATLAS Collaboration), Measurement of the pseudorapidity and transverse momentum dependence of the elliptic flow of charged particles in lead-lead collisions at $\sqrt{s_{NN}} = 2.76$ TeV with the ATLAS detector, Phys. Lett. B **707**, 330 (2012).

[18] J. D. Bjorken, Highly relativistic nucleus-nucleus collisions: The central rapidity region, Phys. Rev. D **27**, 140 (1983).

[19] L. Ahle *et al.* (E-802 Collaboration), Global transverse energy distributions in Si + Al, Au at 14.6 GeV/c and Au + Au at 11.6A GeV/c, Phys. Lett. B **332**, 258 (1994).

[20] J. Barrette *et al.* (E814/E877 Collaboration), Measurement of Transverse Energy Production with Si and Au Beams at Relativistic Energy: Towards Hot and Dense Hadronic Matter, Phys. Rev. Lett. **70**, 2996 (1993).

[21] T. Akesson *et al.* (HELIOS Collaboration), The transverse energy distribution in ^{16}O-nucleus collisions at 60-GeV and 200-GeV per nucleon, Z. Phys. C **38**, 383 (1988).

[22] A. Bamberger *et al.* (NA35 Collaboration), Multiplicity and transverse energy flux in ^{16}O +Pb at 200 GeV per nucleon, Phys. Lett. B **184**, 271 (1987).

[23] T. Alber *et al.* (NA49 Collaboration), Transverse Energy Production in Pb-208 + Pb Collisions at 158-GeV per Nucleon, Phys. Rev. Lett. **75**, 3814 (1995).

[24] R. Albrecht *et al.* (WA80 Collaboration), Distributions of transverse energy and forward energy in O- and S-induced heavy ion collisions at 60A and 200A GeV, Phys. Rev. C **44**, 2736 (1991).

[25] M. Aggarwal *et al.* (WA98 Collaboration), Scaling of particle and transverse energy production in Pb-208 + Pb-208 collisions at 158-A-GeV, Eur. Phys. J. C **18**, 651 (2001).

[26] S. Adler *et al.* (PHENIX Collaboration), Systematic studies of the centrality and $\sqrt{s_{NN}}$ dependence of the $dE_T/d\eta$ and $dN_{ch}/d\eta$ in heavy ion collisions at midrapidity, Phys. Rev. C **71**, 034908 (2005).

[27] K. Adcox *et al.* (PHENIX Collaboration), Measurement of the Mid-Rapidity Transverse Energy Distribution from $\sqrt{s_{NN}} = 130$-GeV Au + Au Collisions at RHIC, Phys. Rev. Lett. **87**, 052301 (2001).

[28] S. Adler *et al.* (PHENIX Collaboration), Transverse-energy distributions at midrapidity in $p + p$, $d +$ Au, and Au + Au collisions at $\sqrt{s_{NN}} = 62.4 - 200$ GeV and implications for particle-production models, Phys. Rev. C **89**, 044905 (2014).

[29] J. Adams *et al.* (STAR Collaboration), Measurements of transverse energy distributions in Au + Au collisions at $\sqrt{s_{NN}} = 200$-GeV, Phys. Rev. C **70**, 054907 (2004).

[30] S. Chatrchyan *et al.* (CMS Collaboration), Measurement of the Pseudorapidity and Centrality Dependence of the Transverse Energy Density in Pb-Pb Collisions at $\sqrt{s} = 2.76$ TeV, Phys. Rev. Lett. **109**, 152303 (2012).

[31] A. Bialas, M. Bleszynski, and W. Czyz, Multiplicity distributions in nucleus-nucleus collisions at high-energies, Nucl. Phys. B **111**, 461 (1976).

[32] M. Miller, K. Reygers, S. Sanders, and P. Steinberg, Glauber modeling in high-energy nuclear collisions, Annu. Rev. Nucl. Part. Sci. **57**, 205 (2007).

[33] X.-N. Wang and M. Gyulassy, Energy and Centrality Dependence of Rapidity Densities at RHIC, Phys. Rev. Lett. **86**, 3496 (2001).

[34] T. A. Trainor, Questioning tests of hadron production models based on minimum-bias distributions on transverse energy, Phys. Rev. C **91**, 044905 (2015).

[35] S. Eremin and S. Voloshin, Nucleon participants or quark participants? Phys. Rev. C **67**, 064905 (2003).

[36] K. Aamodt *et al.* (ALICE Collaboration), The ALICE experiment at the CERN LHC, JINST **3**, S08002 (2008).

[37] E. Abbas *et al.* (ALICE Collaboration), Performance of the ALICE VZERO system, JINST **8**, P10016 (2013).

[38] J. Alme *et al.*, The ALICE TPC, a large 3-dimensional tracking device with fast readout for ultra-high multiplicity events, Nucl. Instrum. Meth. A **622**, 316 (2010).

[39] K. Aamodt *et al.* (ALICE Collaboration), Alignment of the ALICE Inner Tracking System with cosmic-ray tracks, JINST **5**, P03003 (2010).

[40] J. Allen *et al.* (ALICE EMCal Collaboration), Performance of prototypes for the ALICE electromagnetic calorimeter, Nucl. Instrum. Meth. A **615**, 6 (2010).

[41] P. Cortese *et al.* (ALICE Collaboration), ALICE electromagnetic calorimeter technical design report, CERN-LHCC-2008-014; ALICE-TDR-14 (2008).

[42] G. Dellacasa *et al.* (ALICE Collaboration), ALICE technical design report of the photon spectrometer (PHOS), CERN-LHCC-99-04 (1999).

[43] D. V. Aleksandrov *et al.* (ALICE PHOS calorimeter Collaboration), A high resolution electromagnetic calorimeter based on lead-tungstate crystals, Nucl. Instrum. Meth. A **550**, 169 (2005).

[44] B. B. Abelev *et al.* (ALICE Collaboration), Performance of the ALICE Experiment at the CERN LHC, Int. J. Mod. Phys. A **29**, 1430044 (2014).

[45] B. Abelev *et al.* (ALICE Collaboration), Centrality dependence of π, K, p production in Pb-Pb collisions at $\sqrt{s_{NN}} = 2.76$ TeV, Phys. Rev. C **88**, 044910 (2013).

[46] X.-N. Wang and M. Gyulassy, HIJING: A Monte Carlo model for multiple jet production in pp, pA and AA collisions, Phys. Rev. D **44**, 3501 (1991).

[47] R. Brun *et al.*, GEANT Detector Description and Simulation Tool, CERN-W5013, CERN-W-5013, W5013, W-5013 (1993).

[48] B. B. Abelev *et al.* (ALICE Collaboration), K$^*(892)^0$ and $\phi(1020)$ production in Pb-Pb collisions at $\sqrt{s_{NN}} = 2.76$ TeV, Phys. Rev. C **91**, 024609 (2015).

[49] B. B. Abelev *et al.* (ALICE Collaboration), K_S^0 and Λ Production in Pb-Pb Collisions at $\sqrt{s_{NN}} = 2.76$ TeV, Phys. Rev. Lett. **111**, 222301 (2013).

[50] B. B. Abelev *et al.* (ALICE Collaboration), Multiplicity dependence of the average transverse momentum in pp, p-Pb, and Pb-Pb collisions at the LHC, Phys. Lett. B **727**, 371 (2013).

[51] T. Sjostrand, S. Mrenna, and P. Z. Skands, PYTHIA 6.4 physics and manual, J. High Energy Phys 05 (2006) 026.

[52] S. Wheaton and J. Cleymans, THERMUS: A thermal model package for ROOT, Comput. Phys. Commun. **180**, 84 (2009).

[53] A. Adare *et al.* (PHENIX Collaboration), Measurement of neutral mesons in p+p collisions at $\sqrt{s} = 200$ GeV and scaling properties of hadron production, Phys. Rev. D **83**, 052004 (2011).

[54] A. Adare *et al.* (PHENIX Collaboration), Transverse momentum dependence of meson suppression η suppression in Au+Au collisions at $\sqrt{s_{NN}} = 200$ GeV, Phys. Rev. C **82**, 011902 (2010).

[55] B. Abelev *et al.* (ALICE Collaboration), Neutral pion and η meson production in proton-proton collisions at $\sqrt{s} = 0.9$ TeV and $\sqrt{s} = 7$ TeV, Phys. Lett. B **717**, 162 (2012).

[56] K. Aamodt *et al.* (ALICE Collaboration), Midrapidity Antiproton-to-Proton Ratio in pp Collisons at $\sqrt{s} = 0.9$ and

7 TeV Measured by the Alice Experiment, Phys. Rev. Lett. **105**, 072002 (2010).

[57] E. Abbas *et al.* (ALICE Collaboration), Mid-rapidity antibaryon to baryon ratios in pp collisions at $\sqrt{s} = 0.9, 2.76,$ and 7 TeV measured by ALICE, Eur. Phys. J. C **73**, 2496 (2013).

[58] B. Abelev *et al.* (ALICE Collaboration), Centrality determination of Pb-Pb collisions at $\sqrt{s_{NN}} = 2.76$ TeV with ALICE, Phys. Rev. C **88**, 044909 (2013).

[59] B. Abelev *et al.* (ALICE Collaboration), Measurement of the inclusive differential jet cross section in *pp* collisions at $\sqrt{s} = 2.76$ TeV, Phys. Lett. B **722**, 262 (2013).

[60] B. B. Abelev *et al.* (ALICE Collaboration), Neutral pion production at midrapidity in pp and Pb-Pb collisions at $\sqrt{s_{NN}} = 2.76$ TeV, Eur. Phys. J. C **74**, 3108 (2014).

[61] C. Loizides, Glauber modeling of high-energy nuclear collisions at sub-nucleon level, Phys. Rev. C **94**, 024914 (2016).

[62] B. Abelev *et al.* (STAR Collaboration), Systematic Measurements of Identified Particle Spectra in pp, d^+ Au and Au+Au Collisions from STAR, Phys. Rev. C **79**, 034909 (2009).

[63] S. S. Adler *et al.* (PHENIX Collaboration), Identified charged particle spectra and yields in Au + Au collisions at $\sqrt{s_{NN}} = 200$-GeV, Phys. Rev. C **69**, 034909 (2004).

[64] A. Adare *et al.* (PHENIX Collaboration), Transverse energy production and charged-particle multiplicity at midrapidity in various systems from $\sqrt{s_{NN}} = 7.7$ to 200 GeV, Phys. Rev. C **93**, 024901 (2016).

[65] K. Eskola, K. Kajantie, P. Ruuskanen, and K. Tuominen, Scaling of transverse energies and multiplicities with atomic number and energy in ultrarelativistic nuclear collisions, Nucl. Phys. B **570**, 379 (2000).

[66] T. Renk, H. Holopainen, R. Paatelainen, and K. J. Eskola, Systematics of the charged-hadron p_T spectrum and the nuclear suppression factor in heavy-ion collisions from $\sqrt{s} = 200$ GeV to $\sqrt{s} = 2.76$ TeV, Phys. Rev. C **84**, 014906 (2011).

[67] T. Abbott *et al.* (E802 Collaboration), Global transverse energy distributions in relativistic nuclear collisions at 14.6A GeV/c, Phys. Rev. C **45**, 2933 (1992).

[68] Z.-w. Lin, S. Pal, C. Ko, B.-A. Li, and B. Zhang, Charged particle rapidity distributions at relativistic energies, Phys. Rev. C **64**, 011902 (2001).

[69] I. Lokhtin and A. Snigirev, A Model of jet quenching in ultrarelativistic heavy ion collisions and high-p(T) hadron spectra at RHIC, Eur. Phys. J. C **45**, 211 (2006).

[70] J. L. Albacete, A. Dumitru, H. Fujii, and Y. Nara, CGC predictions for p+Pb collisions at the LHC, Nucl. Phys. A **897**, 1 (2013).

[71] B. Alver *et al.*, Importance of correlations and fluctuations on the initial source eccentricity in high-energy nucleus-nucleus collisions, Phys. Rev. C **77**, 014906 (2008).

J. Adam,[39] D. Adamová,[84] M. M. Aggarwal,[88] G. Aglieri Rinella,[35] M. Agnello,[110] N. Agrawal,[47] Z. Ahammed,[133] S. Ahmad,[19] S. U. Ahn,[68] S. Aiola,[137] A. Akindinov,[58] S. N. Alam,[133] D. S. D. Albuquerque,[121] D. Aleksandrov,[80] B. Alessandro,[110] D. Alexandre,[101] R. Alfaro Molina,[64] A. Alici,[12,104] A. Alkin,[3] J. R. M. Almaraz,[119] J. Alme,[37,18] T. Alt,[42] S. Altinpinar,[18] I. Altsybeev,[132] C. Alves Garcia Prado,[120] C. Andrei,[78] A. Andronic,[97] V. Anguelov,[94] T. Antičić,[98] F. Antinori,[107] P. Antonioli,[104] L. Aphecetche,[113] H. Appelshäuser,[53] S. Arcelli,[27] R. Arnaldi,[110] O. W. Arnold,[93,36] I. C. Arsene,[22] M. Arslandok,[53] B. Audurier,[113] A. Augustinus,[35] R. Averbeck,[97] M. D. Azmi,[19] A. Badalà,[106] Y. W. Baek,[67] S. Bagnasco,[110] R. Bailhache,[53] R. Bala,[91] S. Balasubramanian,[137] A. Baldisseri,[15] R. C. Baral,[61] A. M. Barbano,[26] R. Barbera,[28] F. Barile,[32] G. G. Barnaföldi,[136] L. S. Barnby,[101,35] V. Barret,[70] P. Bartalini,[7] K. Barth,[35] J. Bartke,[117] E. Bartsch,[53] M. Basile,[27] N. Bastid,[70] S. Basu,[133] B. Bathen,[54] G. Batigne,[113] A. Batista Camejo,[70] B. Batyunya,[66] P. C. Batzing,[22] I. G. Bearden,[81] H. Beck,[53,94] C. Bedda,[110] N. K. Behera,[48,50] I. Belikov,[55] F. Bellini,[27] H. Bello Martinez,[2] R. Bellwied,[122] R. Belmont,[135] E. Belmont-Moreno,[64] V. Belyaev,[75] G. Bencedi,[136] S. Beole,[26] I. Berceanu,[78] A. Bercuci,[78] Y. Berdnikov,[86] D. Berenyi,[136] R. A. Bertens,[57] D. Berzano,[35] L. Betev,[35] A. Bhasin,[91] I. R. Bhat,[91] A. K. Bhati,[88] B. Bhattacharjee,[44] J. Bhom,[128,117] L. Bianchi,[122] N. Bianchi,[72] C. Bianchin,[135] J. Bielčík,[39] J. Bielčíková,[84] A. Bilandzic,[81,36,93] G. Biro,[136] R. Biswas,[4] S. Biswas,[4,79] S. Bjelogrlic,[57] J. T. Blair,[118] D. Blau,[80] C. Blume,[53] F. Bock,[74,94] A. Bogdanov,[75] H. Bøggild,[81] L. Boldizsár,[136] M. Bombara,[40] J. Book,[53] H. Borel,[15] A. Borissov,[96] M. Borri,[124,83] F. Bossú,[65] E. Botta,[26] C. Bourjau,[81] P. Braun-Munzinger,[97] M. Bregant,[120] T. Breitner,[52] T. A. Broker,[53] T. A. Browning,[95] M. Broz,[39] E. J. Brucken,[45] E. Bruna,[110] G. E. Bruno,[32] D. Budnikov,[99] H. Buesching,[53] S. Bufalino,[35,26] P. Buncic,[35] O. Busch,[128] Z. Buthelezi,[65] J. B. Butt,[16] J. T. Buxton,[20] J. Cabala,[115] D. Caffarri,[35] X. Cai,[7] H. Caines,[137] L. Calero Diaz,[72] A. Caliva,[57] E. Calvo Villar,[102] P. Camerini,[25] F. Carena,[35] W. Carena,[35] F. Carnesecchi,[27] J. Castillo Castellanos,[15] A. J. Castro,[125] E. A. R. Casula,[24] C. Ceballos Sanchez,[9] J. Cepila,[39] P. Cerello,[110] J. Cerkala,[115] B. Chang,[123] S. Chapeland,[35] M. Chartier,[124] J. L. Charvet,[15] S. Chattopadhyay,[133] S. Chattopadhyay,[100] A. Chauvin,[93,36] V. Chelnokov,[3] M. Cherney,[87] C. Cheshkov,[130] B. Cheynis,[130] V. Chibante Barroso,[35] D. D. Chinellato,[121] S. Cho,[50] P. Chochula,[35] K. Choi,[96] M. Chojnacki,[81] S. Choudhury,[133] P. Christakoglou,[82] C. H. Christensen,[81] P. Christiansen,[33] T. Chujo,[128] S. U. Chung,[96] C. Cicalo,[105] L. Cifarelli,[12,27] F. Cindolo,[104] J. Cleymans,[90] F. Colamaria,[32] D. Colella,[59,35] A. Collu,[74] M. Colocci,[27] G. Conesa Balbastre,[71] Z. Conesa del Valle,[51] M. E. Connors,[137,*] J. G. Contreras,[39] T. M. Cormier,[85] Y. Corrales Morales,[110] I. Cortés Maldonado,[2] P. Cortese,[31] M. R. Cosentino,[120] F. Costa,[35] P. Crochet,[70] R. Cruz Albino,[11] E. Cuautle,[63] L. Cunqueiro,[54,35] T. Dahms,[93,36] A. Dainese,[107] M. C. Danisch,[94] A. Danu,[62] D. Das,[100] I. Das,[100] S. Das,[4] A. Dash,[79] S. Dash,[47] S. De,[120] A. De Caro,[12,30] G. de Cataldo,[103] C. de Conti,[120] J. de Cuveland,[42] A. De Falco,[24] D. De Gruttola,[30,12] N. De Marco,[110] S. De Pasquale,[30] A. Deisting,[94,97] A. Deloff,[77] E. Dénes,[136,†] C. Deplano,[82] P. Dhankher,[47] D. Di Bari,[32] A. Di Mauro,[35] P. Di Nezza,[72] M. A. Diaz Corchero,[10] T. Dietel,[90] P. Dillenseger,[53] R. Divià,[35] Ø. Djuvsland,[18] A. Dobrin,[82,62] D. Domenicis Gimenez,[120]

B. Dönigus,[53] O. Dordic,[22] T. Drozhzhova,[53] A. K. Dubey,[133] A. Dubla,[57] L. Ducroux,[130] P. Dupieux,[70] R. J. Ehlers,[137] D. Elia,[103] E. Endress,[102] H. Engel,[52] E. Epple,[93,36,137] B. Erazmus,[113] I. Erdemir,[53] F. Erhardt,[129] B. Espagnon,[51] M. Estienne,[113] S. Esumi,[128] J. Eum,[96] D. Evans,[101] S. Evdokimov,[111] G. Eyyubova,[39] L. Fabbietti,[93,36] D. Fabris,[107] J. Faivre,[71] A. Fantoni,[72] M. Fasel,[74] L. Feldkamp,[54] A. Feliciello,[110] G. Feofilov,[132] J. Ferencei,[84] A. Fernández Téllez,[2] E. G. Ferreiro,[17] A. Ferretti,[26] A. Festanti,[29] V. J. G. Feuillard,[15,70] J. Figiel,[117] M. A. S. Figueredo,[124,120] S. Filchagin,[99] D. Finogeev,[56] F. M. Fionda,[24] E. M. Fiore,[32] M. G. Fleck,[94] M. Floris,[35] S. Foertsch,[65] P. Foka,[97] S. Fokin,[80] E. Fragiacomo,[109] A. Francescon,[35,29] U. Frankenfeld,[97] G. G. Fronze,[26] U. Fuchs,[35] C. Furget,[71] A. Furs,[56] M. Fusco Girard,[30] J. J. Gaardhøje,[81] M. Gagliardi,[26] A. M. Gago,[102] M. Gallio,[26] D. R. Gangadharan,[74] P. Ganoti,[89] C. Gao,[7] C. Garabatos,[97] E. Garcia-Solis,[13] C. Gargiulo,[35] P. Gasik,[93,36] E. F. Gauger,[118] M. Germain,[113] M. Gheata,[35,62] P. Ghosh,[133] S. K. Ghosh,[4] P. Gianotti,[72] P. Giubellino,[110,35] P. Giubilato,[29] E. Gladysz-Dziadus,[117] P. Glässel,[94] D. M. Gómez Coral,[64] A. Gomez Ramirez,[52] A. S. Gonzalez,[35] V. Gonzalez,[10] P. González-Zamora,[10] S. Gorbunov,[42] L. Görlich,[117] S. Gotovac,[116] V. Grabski,[64] O. A. Grachov,[137] L. K. Graczykowski,[134] K. L. Graham,[101] A. Grelli,[57] A. Grigoras,[35] C. Grigoras,[35] V. Grigoriev,[75] A. Grigoryan,[1] S. Grigoryan,[66] B. Grinyov,[3] N. Grion,[109] J. M. Gronefeld,[97] J. F. Grosse-Oetringhaus,[35] R. Grosso,[97] F. Guber,[56] R. Guernane,[71] B. Guerzoni,[27] K. Gulbrandsen,[81] T. Gunji,[127] A. Gupta,[91] R. Gupta,[91] R. Haake,[35] Ø. Haaland,[18] C. Hadjidakis,[51] M. Haiduc,[62] H. Hamagaki,[127] G. Hamar,[136] J. C. Hamon,[55] J. W. Harris,[137] A. Harton,[13] D. Hatzifotiadou,[104] S. Hayashi,[127] S. T. Heckel,[53] E. Hellbär,[53] H. Helstrup,[37] A. Herghelegiu,[78] G. Herrera Corral,[11] B. A. Hess,[34] K. F. Hetland,[37] H. Hillemanns,[35] B. Hippolyte,[55] D. Horak,[39] R. Hosokawa,[128] P. Hristov,[35] T. J. Humanic,[20] N. Hussain,[44] T. Hussain,[19] D. Hutter,[42] D. S. Hwang,[21] R. Ilkaev,[99] M. Inaba,[128] E. Incani,[24] M. Ippolitov,[75,80] M. Irfan,[19] M. Ivanov,[97] V. Ivanov,[86] V. Izucheev,[111] N. Jacazio,[27] P. M. Jacobs,[74] M. B. Jadhav,[47] S. Jadlovska,[115] J. Jadlovsky,[115,59] C. Jahnke,[120] M. J. Jakubowska,[134] H. J. Jang,[68] M. A. Janik,[134] P. H. S. Y. Jayarathna,[122] C. Jena,[29] S. Jena,[122] R. T. Jimenez Bustamante,[97] P. G. Jones,[101] A. Jusko,[101] P. Kalinak,[59] A. Kalweit,[35] J. Kamin,[53] J. H. Kang,[138] V. Kaplin,[75] S. Kar,[133] A. Karasu Uysal,[69] O. Karavichev,[56] T. Karavicheva,[56] L. Karayan,[97,94] E. Karpechev,[56] U. Kebschull,[52] R. Keidel,[139] D. L. D. Keijdener,[57] M. Keil,[35] M. Mohisin Khan,[19,‡] P. Khan,[100] S. A. Khan,[133] A. Khanzadeev,[86] Y. Kharlov,[111] B. Kileng,[37] D. W. Kim,[43] D. J. Kim,[123] D. Kim,[138] H. Kim,[138] J. S. Kim,[43] M. Kim,[138] S. Kim,[21] T. Kim,[138] S. Kirsch,[42] I. Kisel,[42] S. Kiselev,[58] A. Kisiel,[134] G. Kiss,[136] J. L. Klay,[6] C. Klein,[53] J. Klein,[35] C. Klein-Bösing,[54] S. Klewin,[94] A. Kluge,[35] M. L. Knichel,[94] A. G. Knospe,[118,122] C. Kobdaj,[114] M. Kofarago,[35] T. Kollegger,[97] A. Kolojvari,[132] V. Kondratiev,[132] N. Kondratyeva,[75] E. Kondratyuk,[111] A. Konevskikh,[56] M. Kopcik,[115] P. Kostarakis,[89] M. Kour,[91] C. Kouzinopoulos,[35] O. Kovalenko,[77] V. Kovalenko,[132] M. Kowalski,[117] G. Koyithatta Meethaleveedu,[47] I. Králik,[59] A. Kravčáková,[40] M. Krivda,[59,101] F. Krizek,[84] E. Kryshen,[86,35] M. Krzewicki,[42] A. M. Kubera,[20] V. Kučera,[84] C. Kuhn,[55] P. G. Kuijer,[82] A. Kumar,[91] J. Kumar,[47] L. Kumar,[88] S. Kumar,[47] P. Kurashvili,[77] A. Kurepin,[56] A. B. Kurepin,[56] A. Kuryakin,[99] M. J. Kweon,[50] Y. Kwon,[138] S. L. La Pointe,[110] P. La Rocca,[28] P. Ladron de Guevara,[11] C. Lagana Fernandes,[120] I. Lakomov,[35] R. Langoy,[41] K. Lapidus,[93,36] C. Lara,[52] A. Lardeux,[15] A. Lattuca,[26] E. Laudi,[35] R. Lea,[25] L. Leardini,[94] G. R. Lee,[101] S. Lee,[138] F. Lehas,[82] R. C. Lemmon,[83] V. Lenti,[103] E. Leogrande,[57] I. León Monzón,[119] H. León Vargas,[64] M. Leoncino,[26] P. Lévai,[136] S. Li,[7,70] X. Li,[14] J. Lien,[41] R. Lietava,[101] S. Lindal,[22] V. Lindenstruth,[42] C. Lippmann,[97] M. A. Lisa,[20] H. M. Ljunggren,[33] D. F. Lodato,[57] P. I. Loenne,[18] V. Loginov,[75] C. Loizides,[74] X. Lopez,[70] E. López Torres,[9] A. Lowe,[136] P. Luettig,[53] M. Lunardon,[29] G. Luparello,[25] T. H. Lutz,[137] A. Maevskaya,[56] M. Mager,[35] S. Mahajan,[91] S. M. Mahmood,[22] A. Maire,[55] R. D. Majka,[137] M. Malaev,[86] I. Maldonado Cervantes,[63] L. Malinina,[66,§] D. Mal'Kevich,[58] P. Malzacher,[97] A. Mamonov,[99] V. Manko,[80] F. Manso,[70] V. Manzari,[35,103] M. Marchisone,[26,65,126] J. Mareš,[60] G. V. Margagliotti,[25] A. Margotti,[104] J. Margutti,[57] A. Marín,[97] C. Markert,[118] M. Marquard,[53] N. A. Martin,[97] J. Martin Blanco,[113] P. Martinengo,[35] M. I. Martínez,[2] G. Martínez García,[113] M. Martinez Pedreira,[35] A. Mas,[120] S. Masciocchi,[97] M. Masera,[26] A. Masoni,[105] A. Mastroserio,[32] A. Matyja,[117] C. Mayer,[117] J. Mazer,[125] M. A. Mazzoni,[108] D. Mcdonald,[122] F. Meddi,[23] Y. Melikyan,[75] A. Menchaca-Rocha,[64] E. Meninno,[30] J. Mercado Pérez,[94] M. Meres,[38] Y. Miake,[128] M. M. Mieskolainen,[45] K. Mikhaylov,[58,66] L. Milano,[74,35] J. Milosevic,[22] A. Mischke,[57] A. N. Mishra,[48] D. Miśkowiec,[97] J. Mitra,[133] C. M. Mitu,[62] N. Mohammadi,[57] B. Mohanty,[79] L. Molnar,[55] L. Montaño Zetina,[11] E. Montes,[10] D. A. Moreira De Godoy,[54] L. A. P. Moreno,[2] S. Moretto,[29] A. Morreale,[113] A. Morsch,[35] V. Muccifora,[72] E. Mudnic,[116] D. Mühlheim,[54] S. Muhuri,[133] M. Mukherjee,[133] J. D. Mulligan,[137] M. G. Munhoz,[120] R. H. Munzer,[53,93,36] H. Murakami,[127] S. Murray,[65] L. Musa,[35] J. Musinsky,[59] B. Naik,[47] R. Nair,[77] B. K. Nandi,[47] R. Nania,[104] E. Nappi,[103] M. U. Naru,[16] H. Natal da Luz,[120] C. Nattrass,[125] S. R. Navarro,[2] K. Nayak,[79] R. Nayak,[47] T. K. Nayak,[133] S. Nazarenko,[99] A. Nedosekin,[58] L. Nellen,[63] F. Ng,[122] M. Nicassio,[97] M. Niculescu,[62] J. Niedziela,[35] B. S. Nielsen,[81] S. Nikolaev,[80] S. Nikulin,[80] V. Nikulin,[86] F. Noferini,[104,12] P. Nomokonov,[66] G. Nooren,[57] J. C. C. Noris,[2] J. Norman,[124] A. Nyanin,[80] J. Nystrand,[18] H. Oeschler,[94] S. Oh,[137] S. K. Oh,[67] A. Ohlson,[35] A. Okatan,[69] T. Okubo,[46] L. Olah,[136] J. Oleniacz,[134] A. C. Oliveira Da Silva,[120] M. H. Oliver,[137] J. Onderwaater,[97] C. Oppedisano,[110] R. Orava,[45] M. Oravec,[115] A. Ortiz Velasquez,[63] A. Oskarsson,[33] J. Otwinowski,[117] K. Oyama,[94,76] Y. Pachmayer,[94] D. Pagano,[131] P. Pagano,[30] G. Paić,[63] S. K. Pal,[133] J. Pan,[135] A. K. Pandey,[47] V. Papikyan,[1] G. S. Pappalardo,[106] P. Pareek,[48] W. J. Park,[97] S. Parmar,[88] A. Passfeld,[54] V. Paticchio,[103] R. N. Patra,[133] B. Paul,[100,110] H. Pei,[7] T. Peitzmann,[57] H. Pereira Da Costa,[15] D. Peresunko,[80,75] C. E. Pérez Lara,[82] E. Perez Lezama,[53] V. Peskov,[53] Y. Pestov,[5] V. Petráček,[39] V. Petrov,[111] M. Petrovici,[78] C. Petta,[28] S. Piano,[109] M. Pikna,[38] P. Pillot,[113] L. O. D. L. Pimentel,[81] O. Pinazza,[104,35] L. Pinsky,[122] D. B. Piyarathna,[122] M. Płoskoń,[74] M. Planinic,[129] J. Pluta,[134] S. Pochybova,[136] P. L. M. Podesta-Lerma,[119] M. G. Poghosyan,[85,87] B. Polichtchouk,[111] N. Poljak,[129] W. Poonsawat,[114] A. Pop,[78] S. Porteboeuf-Houssais,[70] J. Porter,[74] J. Pospisil,[84] S. K. Prasad,[4]

R. Preghenella,[104,35] F. Prino,[110] C. A. Pruneau,[135] I. Pshenichnov,[56] M. Puccio,[26] G. Puddu,[24] P. Pujahari,[135] V. Punin,[99] J. Putschke,[135] H. Qvigstad,[22] A. Rachevski,[109] S. Raha,[4] S. Rajput,[91] J. Rak,[123] A. Rakotozafindrabe,[15] L. Ramello,[31] F. Rami,[55] R. Raniwala,[92] S. Raniwala,[92] S. S. Räsänen,[45] B. T. Rascanu,[53] D. Rathee,[88] K. F. Read,[85,125] K. Redlich,[77] R. J. Reed,[135] A. Rehman,[18] P. Reichelt,[53] F. Reidt,[35,94] X. Ren,[7] R. Renfordt,[53] A. R. Reolon,[72] A. Reshetin,[56] K. Reygers,[94] V. Riabov,[86] R. A. Ricci,[73] T. Richert,[33] M. Richter,[22] P. Riedler,[35] W. Riegler,[35] F. Riggi,[28] C. Ristea,[62] E. Rocco,[57] M. Rodríguez Cahuantzi,[11,2] A. Rodriguez Manso,[82] K. Røed,[22] E. Rogochaya,[66] D. Rohr,[42] D. Röhrich,[18] F. Ronchetti,[35,72] L. Ronflette,[113] P. Rosnet,[70] A. Rossi,[29,35] F. Roukoutakis,[89] A. Roy,[48] C. Roy,[55] P. Roy,[100] A. J. Rubio Montero,[10] R. Rui,[25] R. Russo,[26] B. D. Ruzza,[107] E. Ryabinkin,[80] Y. Ryabov,[86] A. Rybicki,[117] S. Saarinen,[45] S. Sadhu,[133] S. Sadovsky,[111] K. Šafařík,[35] B. Sahlmuller,[53] P. Sahoo,[48] R. Sahoo,[48] S. Sahoo,[61] P. K. Sahu,[61] J. Saini,[133] S. Sakai,[72] M. A. Saleh,[135] J. Salzwedel,[20] S. Sambyal,[91] V. Samsonov,[86] L. Šándor,[59] A. Sandoval,[64] M. Sano,[128] D. Sarkar,[133] N. Sarkar,[133] P. Sarma,[44] E. Scapparone,[104] F. Scarlassara,[29] C. Schiaua,[78] R. Schicker,[94] C. Schmidt,[97] H. R. Schmidt,[34] S. Schuchmann,[53] J. Schukraft,[35] M. Schulc,[39] Y. Schutz,[35,113] K. Schwarz,[97] K. Schweda,[97] G. Scioli,[27] E. Scomparin,[110] R. Scott,[125] M. Šefčík,[40] J. E. Seger,[87] Y. Sekiguchi,[127] D. Sekihata,[46] I. Selyuzhenkov,[97] K. Senosi,[65] S. Senyukov,[35,3] E. Serradilla,[10,64] A. Sevcenco,[62] A. Shabanov,[56] A. Shabetai,[113] O. Shadura,[3] R. Shahoyan,[35] M. I. Shahzad,[16] A. Shangaraev,[111] A. Sharma,[91] M. Sharma,[91] M. Sharma,[91] N. Sharma,[125] A. I. Sheikh,[133] K. Shigaki,[46] Q. Shou,[7] K. Shtejer,[9,26] Y. Sibiriak,[80] S. Siddhanta,[105] K. M. Sielewicz,[35] T. Siemiarczuk,[77] D. Silvermyr,[33] C. Silvestre,[71] G. Simatovic,[129] G. Simonetti,[35] R. Singaraju,[133] R. Singh,[79] S. Singha,[79,133] V. Singhal,[133] B. C. Sinha,[133] T. Sinha,[100] B. Sitar,[38] M. Sitta,[31] T. B. Skaali,[22] M. Slupecki,[123] N. Smirnov,[137] R. J. M. Snellings,[57] T. W. Snellman,[123] J. Song,[96] M. Song,[138] Z. Song,[7] F. Soramel,[29] S. Sorensen,[125] R. D. de Souza,[121] F. Sozzi,[97] M. Spacek,[39] E. Spiriti,[72] I. Sputowska,[117] M. Spyropoulou-Stassinaki,[89] J. Stachel,[94] I. Stan,[62] P. Stankus,[85] E. Stenlund,[33] G. Steyn,[65] J. H. Stiller,[94] D. Stocco,[113] P. Strmen,[38] A. A. P. Suaide,[120] T. Sugitate,[46] C. Suire,[51] M. Suleymanov,[16] M. Suljic,[25,†] R. Sultanov,[58] M. Šumbera,[84] S. Sumowidagdo,[49] A. Szabo,[38] A. Szanto de Toledo,[120,†] I. Szarka,[38] A. Szczepankiewicz,[35] M. Szymanski,[134] U. Tabassam,[16] J. Takahashi,[121] G. J. Tambave,[18] N. Tanaka,[128] M. Tarhini,[51] M. Tariq,[19] M. G. Tarzila,[78] A. Tauro,[35] G. Tejeda Muñoz,[2] A. Telesca,[35] K. Terasaki,[127] C. Terrevoli,[29] B. Teyssier,[130] J. Thäder,[74] D. Thakur,[48] D. Thomas,[118] R. Tieulent,[130] A. Tikhonov,[56] A. R. Timmins,[122] A. Toia,[53] S. Trogolo,[26] G. Trombetta,[32] V. Trubnikov,[3] W. H. Trzaska,[123] T. Tsuji,[127] A. Tumkin,[99] R. Turrisi,[107] T. S. Tveter,[22] K. Ullaland,[18] A. Uras,[130] G. L. Usai,[24] A. Utrobicic,[129] M. Vala,[59] L. Valencia Palomo,[70] S. Vallero,[26] J. Van Der Maarel,[57] J. W. Van Hoorne,[35] M. van Leeuwen,[57] T. Vanat,[84] P. Vande Vyvre,[35] D. Varga,[136] A. Vargas,[2] M. Vargyas,[123] R. Varma,[47] M. Vasileiou,[89] A. Vasiliev,[80] A. Vauthier,[71] O. Vázquez Doce,[36,93] V. Vechernin,[132] A. M. Veen,[57] M. Veldhoen,[57] A. Velure,[18] E. Vercellin,[26] S. Vergara Limón,[2] R. Vernet,[8] M. Verweij,[135] L. Vickovic,[116] J. Viinikainen,[123] Z. Vilakazi,[126] O. Villalobos Baillie,[101] A. Villatoro Tello,[2] A. Vinogradov,[80] L. Vinogradov,[132] Y. Vinogradov,[99,†] T. Virgili,[30] V. Vislavicius,[33] Y.P. Viyogi,[133] A. Vodopyanov,[66] M. A. Völkl,[94] K. Voloshin,[58] S. A. Voloshin,[135] G. Volpe,[32,136] B. von Haller,[35] I. Vorobyev,[93,36] D. Vranic,[97,35] J. Vrláková,[40] B. Vulpescu,[70] B. Wagner,[18] J. Wagner,[97] H. Wang,[57] M. Wang,[7,113] D. Watanabe,[128] Y. Watanabe,[127] M. Weber,[112,35] S. G. Weber,[97] D. F. Weiser,[94] J. P. Wessels,[54] U. Westerhoff,[54] A. M. Whitehead,[90] J. Wiechula,[34] J. Wikne,[22] G. Wilk,[77] J. Wilkinson,[94] M. C. S. Williams,[104] B. Windelband,[94] M. Winn,[94] P. Yang,[7] S. Yano,[46] Z. Yasin,[16] Z. Yin,[7] H. Yokoyama,[128] I.-K. Yoo,[96] J. H. Yoon,[50] V. Yurchenko,[3] I. Yushmanov,[80] A. Zaborowska,[134] V. Zaccolo,[81] A. Zaman,[16] C. Zampolli,[104,35] H. J. C. Zanoli,[120] S. Zaporozhets,[66] N. Zardoshti,[101] A. Zarochentsev,[132] P. Závada,[60] N. Zaviyalov,[99] H. Zbroszczyk,[134] I. S. Zgura,[62] M. Zhalov,[86] H. Zhang,[18] X. Zhang,[74,7] Y. Zhang,[7] C. Zhang,[57] Z. Zhang,[7] C. Zhao,[22] N. Zhigareva,[58] D. Zhou,[7] Y. Zhou,[81] Z. Zhou,[18] H. Zhu,[18] J. Zhu,[7,113] A. Zichichi,[27,12] A. Zimmermann,[94] M. B. Zimmermann,[54,35] G. Zinovjev,[3] and M. Zyzak[42]

(ALICE Collaboration)

[1]*A. I. Alikhanyan National Science Laboratory (Yerevan Physics Institute) Foundation, Yerevan, Armenia*
[2]*Benemérita Universidad Autónoma de Puebla, Puebla, Mexico*
[3]*Bogolyubov Institute for Theoretical Physics, Kiev, Ukraine*
[4]*Bose Institute, Department of Physics and Centre for Astroparticle Physics and Space Science (CAPSS), Kolkata, India*
[5]*Budker Institute for Nuclear Physics, Novosibirsk, Russia*
[6]*California Polytechnic State University, San Luis Obispo, California 93407, USA*
[7]*Central China Normal University, Wuhan, China*
[8]*Centre de Calcul de l'IN2P3, Villeurbanne, France*
[9]*Centro de Aplicaciones Tecnológicas y Desarrollo Nuclear (CEADEN), Havana, Cuba*
[10]*Centro de Investigaciones Energéticas Medioambientales y Tecnológicas (CIEMAT), Madrid, Spain*
[11]*Centro de Investigación y de Estudios Avanzados (CINVESTAV), Mexico City and Mérida, Mexico*
[12]*Centro Fermi-Museo Storico della Fisica e Centro Studi e Ricerche "Enrico Fermi," Rome, Italy*
[13]*Chicago State University, Chicago, Illinois 60628, USA*
[14]*China Institute of Atomic Energy, Beijing, China*
[15]*Commissariat à l'Energie Atomique, IRFU, Saclay, France*
[16]*COMSATS Institute of Information Technology (CIIT), Islamabad, Pakistan*

[17]*Departamento de Física de Partículas and IGFAE, Universidad de Santiago de Compostela, Santiago de Compostela, Spain*
[18]*Department of Physics and Technology, University of Bergen, Bergen, Norway*
[19]*Department of Physics, Aligarh Muslim University, Aligarh, India*
[20]*Department of Physics, Ohio State University, Columbus, Ohio 43210, USA*
[21]*Department of Physics, Sejong University, Seoul, South Korea*
[22]*Department of Physics, University of Oslo, Oslo, Norway*
[23]*Dipartimento di Fisica dell'Università "La Sapienza" and Sezione INFN Rome, Italy*
[24]*Dipartimento di Fisica dell'Università and Sezione INFN, Cagliari, Italy*
[25]*Dipartimento di Fisica dell'Università and Sezione INFN, Trieste, Italy*
[26]*Dipartimento di Fisica dell'Università and Sezione INFN, Turin, Italy*
[27]*Dipartimento di Fisica e Astronomia dell'Università and Sezione INFN, Bologna, Italy*
[28]*Dipartimento di Fisica e Astronomia dell'Università and Sezione INFN, Catania, Italy*
[29]*Dipartimento di Fisica e Astronomia dell'Università and Sezione INFN, Padova, Italy*
[30]*Dipartimento di Fisica "E. R. Caianiello" dell'Università and Gruppo Collegato INFN, Salerno, Italy*
[31]*Dipartimento di Scienze e Innovazione Tecnologica dell'Università del Piemonte Orientale and Gruppo Collegato INFN, Alessandria, Italy*
[32]*Dipartimento Interateneo di Fisica "M. Merlin" and Sezione INFN, Bari, Italy*
[33]*Division of Experimental High Energy Physics, University of Lund, Lund, Sweden*
[34]*Eberhard Karls Universität Tübingen, Tübingen, Germany*
[35]*European Organization for Nuclear Research (CERN), Geneva, Switzerland*
[36]*Excellence Cluster Universe, Technische Universität München, Munich, Germany*
[37]*Faculty of Engineering, Bergen University College, Bergen, Norway*
[38]*Faculty of Mathematics, Physics and Informatics, Comenius University, Bratislava, Slovakia*
[39]*Faculty of Nuclear Sciences and Physical Engineering, Czech Technical University in Prague, Prague, Czech Republic*
[40]*Faculty of Science, P. J. Šafárik University, Košice, Slovakia*
[41]*Faculty of Technology, Buskerud and Vestfold University College, Vestfold, Norway*
[42]*Frankfurt Institute for Advanced Studies, Johann Wolfgang Goethe-Universität Frankfurt, Frankfurt, Germany*
[43]*Gangneung-Wonju National University, Gangneung, South Korea*
[44]*Gauhati University, Department of Physics, Guwahati, India*
[45]*Helsinki Institute of Physics (HIP), Helsinki, Finland*
[46]*Hiroshima University, Hiroshima, Japan*
[47]*Indian Institute of Technology Bombay (IIT), Mumbai, India*
[48]*Indian Institute of Technology Indore, Indore (IITI), India*
[49]*Indonesian Institute of Sciences, Jakarta, Indonesia*
[50]*Inha University, Incheon, South Korea*
[51]*Institut de Physique Nucléaire d'Orsay (IPNO), Université Paris-Sud, CNRS-IN2P3, Orsay, France*
[52]*Institut für Informatik, Johann Wolfgang Goethe-Universität Frankfurt, Frankfurt, Germany*
[53]*Institut für Kernphysik, Johann Wolfgang Goethe-Universität Frankfurt, Frankfurt, Germany*
[54]*Institut für Kernphysik, Westfälische Wilhelms-Universität Münster, Münster, Germany*
[55]*Institut Pluridisciplinaire Hubert Curien (IPHC), Université de Strasbourg, CNRS-IN2P3, Strasbourg, France*
[56]*Institute for Nuclear Research, Academy of Sciences, Moscow, Russia*
[57]*Institute for Subatomic Physics of Utrecht University, Utrecht, Netherlands*
[58]*Institute for Theoretical and Experimental Physics, Moscow, Russia*
[59]*Institute of Experimental Physics, Slovak Academy of Sciences, Košice, Slovakia*
[60]*Institute of Physics, Academy of Sciences of the Czech Republic, Prague, Czech Republic*
[61]*Institute of Physics, Bhubaneswar, India*
[62]*Institute of Space Science (ISS), Bucharest, Romania*
[63]*Instituto de Ciencias Nucleares, Universidad Nacional Autónoma de México, Mexico City, Mexico*
[64]*Instituto de Física, Universidad Nacional Autónoma de México, Mexico City, Mexico*
[65]*iThemba LABS, National Research Foundation, Somerset West, South Africa*
[66]*Joint Institute for Nuclear Research (JINR), Dubna, Russia*
[67]*Konkuk University, Seoul, South Korea*
[68]*Korea Institute of Science and Technology Information, Daejeon, South Korea*
[69]*KTO Karatay University, Konya, Turkey*
[70]*Laboratoire de Physique Corpusculaire (LPC), Clermont Université, Université Blaise Pascal, CNRS–IN2P3, Clermont-Ferrand, France*
[71]*Laboratoire de Physique Subatomique et de Cosmologie, Université Grenoble-Alpes, CNRS-IN2P3, Grenoble, France*
[72]*Laboratori Nazionali di Frascati, INFN, Frascati, Italy*
[73]*Laboratori Nazionali di Legnaro, INFN, Legnaro, Italy*
[74]*Lawrence Berkeley National Laboratory, Berkeley, California 94720, USA*
[75]*Moscow Engineering Physics Institute, Moscow, Russia*

[76]*Nagasaki Institute of Applied Science, Nagasaki, Japan*
[77]*National Centre for Nuclear Studies, Warsaw, Poland*
[78]*National Institute for Physics and Nuclear Engineering, Bucharest, Romania*
[79]*National Institute of Science Education and Research, Bhubaneswar, India*
[80]*National Research Centre Kurchatov Institute, Moscow, Russia*
[81]*Niels Bohr Institute, University of Copenhagen, Copenhagen, Denmark*
[82]*Nikhef, Nationaal instituut voor subatomaire fysica, Amsterdam, Netherlands*
[83]*Nuclear Physics Group, STFC Daresbury Laboratory, Daresbury, United Kingdom*
[84]*Nuclear Physics Institute, Academy of Sciences of the Czech Republic, Řež u Prahy, Czech Republic*
[85]*Oak Ridge National Laboratory, Oak Ridge, Tennessee 37831, USA*
[86]*Petersburg Nuclear Physics Institute, Gatchina, Russia*
[87]*Physics Department, Creighton University, Omaha, Nebraska 68178, USA*
[88]*Physics Department, Panjab University, Chandigarh, India*
[89]*Physics Department, University of Athens, Athens, Greece*
[90]*Physics Department, University of Cape Town, Cape Town, South Africa*
[91]*Physics Department, University of Jammu, Jammu, India*
[92]*Physics Department, University of Rajasthan, Jaipur, India*
[93]*Physik Department, Technische Universität München, Munich, Germany*
[94]*Physikalisches Institut, Ruprecht-Karls-Universität Heidelberg, Heidelberg, Germany*
[95]*Purdue University, West Lafayette, Indiana 47907, USA*
[96]*Pusan National University, Pusan, South Korea*
[97]*Research Division and ExtreMe Matter Institute EMMI, GSI Helmholtzzentrum für Schwerionenforschung, Darmstadt, Germany*
[98]*Rudjer Bošković Institute, Zagreb, Croatia*
[99]*Russian Federal Nuclear Center (VNIIEF), Sarov, Russia*
[100]*Saha Institute of Nuclear Physics, Kolkata, India*
[101]*School of Physics and Astronomy, University of Birmingham, Birmingham, United Kingdom*
[102]*Sección Física, Departamento de Ciencias, Pontificia Universidad Católica del Perú, Lima, Peru*
[103]*Sezione INFN, Bari, Italy*
[104]*Sezione INFN, Bologna, Italy*
[105]*Sezione INFN, Cagliari, Italy*
[106]*Sezione INFN, Catania, Italy*
[107]*Sezione INFN, Padova, Italy*
[108]*Sezione INFN, Rome, Italy*
[109]*Sezione INFN, Trieste, Italy*
[110]*Sezione INFN, Turin, Italy*
[111]*SSC IHEP of NRC Kurchatov institute, Protvino, Russia*
[112]*Stefan Meyer Institut für Subatomare Physik (SMI), Vienna, Austria*
[113]*SUBATECH, Ecole des Mines de Nantes, Université de Nantes, CNRS-IN2P3, Nantes, France*
[114]*Suranaree University of Technology, Nakhon Ratchasima, Thailand*
[115]*Technical University of Košice, Košice, Slovakia*
[116]*Technical University of Split FESB, Split, Croatia*
[117]*The Henryk Niewodniczanski Institute of Nuclear Physics, Polish Academy of Sciences, Cracow, Poland*
[118]*Physics Department, The University of Texas at Austin, Austin, Texas 78712, USA*
[119]*Universidad Autónoma de Sinaloa, Culiacán, Mexico*
[120]*Universidade de São Paulo (USP), São Paulo, Brazil*
[121]*Universidade Estadual de Campinas (UNICAMP), Campinas, Brazil*
[122]*University of Houston, Houston, Texas 77004, USA*
[123]*University of Jyväskylä, Jyväskylä, Finland*
[124]*University of Liverpool, Liverpool, United Kingdom*
[125]*University of Tennessee, Knoxville, Tennessee 37996, USA*
[126]*University of the Witwatersrand, Johannesburg, South Africa*
[127]*University of Tokyo, Tokyo, Japan*
[128]*University of Tsukuba, Tsukuba, Japan*
[129]*University of Zagreb, Zagreb, Croatia*
[130]*Université de Lyon, Université Lyon 1, CNRS/IN2P3, IPN-Lyon, Villeurbanne, France*
[131]*Università di Brescia, Brescia, Italy*
[132]*V. Fock Institute for Physics, St. Petersburg State University, St. Petersburg, Russia*
[133]*Variable Energy Cyclotron Centre, Kolkata, India*
[134]*Warsaw University of Technology, Warsaw, Poland*

[135]*Wayne State University, Detroit, Michigan 48202, USA*

[136]*Wigner Research Centre for Physics, Hungarian Academy of Sciences, Budapest, Hungary*

[137]*Yale University, New Haven, Connecticut 06520, USA*

[138]*Yonsei University, Seoul, South Korea*

[139]*Zentrum für Technologietransfer und Telekommunikation (ZTT), Fachhochschule Worms, Worms, Germany*

[*]Also at: Georgia State University, Atlanta, Georgia, United States.

[†]Deceased.

[‡]Also at: Department of Applied Physics, Aligarh Muslim University, Aligarh, India.

[§]Also at: M.V. Lomonosov Moscow State University, D.V. Skobeltsyn Institute of Nuclear, Physics, Moscow, Russia.